TECHNICAL ARTICLE

An Experimental and Statistical Analysis on Dry Sliding Wear Failure Behavior of Incoloy 825 at Elevated Temperatures

Faruk Çavdar, Ali Günen [ID] *, Erdoğan Kanca, Yusuf Er, Mustafa Sabri Gök, Ivan Campos-Silva, and M. Olivares-Luna*

Incoloy 825 is a Ni-Fe-Co superalloy which is used at temperatures in a wide range of temperatures from room temperatures to 650 °C. To overcome difficulty of testing of wear properties of the material in this wide range, Response Surface Methodology is used to assess the wear behaviors such as coefficient of friction (CoF), wear track area and specific wear rate under varying dry sliding test variables such as sliding speed, load and especially temperature. Central composite design was performed to determine experimental sets of independent parameters. Dry sliding wear tests with these parameter sets were carried out on the Incoloy 825. The response surfaces constructed by using these test results revealed that the temperature, load, and speed affect response variables in a complex way. The CoF is negatively influenced by increase in load and speed, but the CoF behaves in adverse manner in high temperatures, as shown by the established response model. Wear track area tends to decrease as the temperature rises up to 650 °C. In high temperatures, the wear rate reduces as the load increases, but it rises when the sliding speed increases. SEM and EDS analyses showed that the wear behavior changed from plastic deformation to oxidation type wear mechanism with the increase in temperature, load and speed.

1. Introduction

Superalloys are critical high-temperature engineering materials. The superalloys originated from the development of austenitic stainless steels between 1950 and 1970. The difference of superalloys from stainless steels is that they contain elements such as Ni, Cr, Ni, Mo, Ti at a higher rate (Ref 1-3). Although the prices of these elements are higher than Fe,

Faruk Çavdar, Department of Machinery and Metal Technologies, Osmaniye Vocational School, Osmaniye Korkut Ata University, Osmaniye, Türkiye; **Ali Günen**, Department of Metallurgy and Materials Engineering, Faculty of Engineering and Natural Sciences, Iskenderun Technical University, 31200 Hatay, Türkiye; **Erdoğan Kanca**, Department of Mechanical Engineering, Faculty of Engineering and Natural Sciences, Iskenderun Technical University, 31200 Hatay, Türkiye; **Yusuf Er**, Department of Airframe-Engine, School of Civil Aviation, Fırat University, 23000 Elazığ, Türkiye; **Mustafa Sabri Gök**, Department of Mechanical Engineering, Faculty of Engineering, Architecture and Design, Bartın University, 74000 Bartın, Türkiye; and **Ivan Campos-Silva** and **M. Olivares-Luna**, Grupo Ingeniería de Superficies, Instituto Politécnico Nacional, SEPI-ESIME, U.P. Adolfo López Mateos, 07738 Zacatenco, Mexico City, Mexico. Contact e-mail: ali.gunen@iste.edu.tr.

they give unique properties to superalloys. That is, while Ni addition provides resistance to chloride-iron stress-corrosion cracking, when Ni and Mo are doped together, they ensure resistance against reducing environments and pitting corrosion. Existence of Cr provides resistance to various oxidizing agents such as nitric acid, nitrate, and oxidizing salts, while Ti stabilizes the susceptibility to intergranular corrosion (Ref 3-5).

Superalloys are generally classified as Ni-based superalloys, Co-based superalloys and Iron-based superalloys depending on the base element that makes up their content. However, in alloys such as Incoloy 825, where the elements in the alloy are close to each other, they can also be named by giving the names of the three elements with the highest ratio forming the chemical composition (Ref 6).

For high temperature applications (> 700 °C), nickel- and cobalt-based superalloys are favored, while iron-based superalloys are extensively employed in intermediate temperature applications (650 °C). Incoloy 825 alloy is one of the superalloys called Ni-Cr-Fe alloy, which is in the chemical composition ranges of Ni- and Fe-based superalloys (Ref 3, 7). The Incoloy 825 alloy, which is based on Ni-Fe-Cr, is a solid-solution-strengthened superalloy that is extensively used in critical applications due to its superior resistance to uniform local corrosion in diverse atmospheres and the ability to maintain a high mechanical stability over a wide temperature range (Ref 8, 9).

Considering the wide usage area of Incoloy 825 alloy such as chemical processing, oil and gas recovery, pickling operations, acid production, handling of radioactive wastes and nuclear fuel reprocessing (Ref 10), it has been determined that this alloy is widely used at temperatures from room temperature to 650 °C. During literature surveys, it has been determined that although there are many studies on weldability, machinability, and corrosion resistance (Ref 11-13) but studies on wear

behavior are limited. Therefore, it is of great importance to understand the wear behavior of this alloy in the specified temperature ranges. Because, it is stated that the cost of energy and material loss due to abrasion in the world is over 2500 Billion Euros per year.

Although Incoloy 825 is used in tribocorrosive environments with wide range compelling factors such as temperature, load and sliding speed (s), there is a lack of systematic studies found in the literature to determine wear behavior of this material. To determine wear behavior in a wide range of varying conditions, wear tests require multiple iterations to cover all application areas. This problem can be solved by using appropriate experimental designs with determination of cost-effective parameter ranges and developing proper regression models. So that wear behavior of the material can be predicted in concerned conditions without making trials. RSM is one of the tools used in developing a regression model, and it is a method that has proven its effectiveness and has a wide range of uses. For this reason, considering abrasive working environments, wear behavior i.e., coefficient of friction (CoF), wear track area (A), and specific wear rate (SWR), of Incoloy 825 under varying conditions i.e., temperatures between 25 and 650 °C, sliding speed between 150 and 250 mm/s and load between 5 and 20 N was investigated in this study.

2. Materials and Method

2.1 Experiment Design for Response Surfaces

First stage of the response surface methodology is determination of independent parameters that influences the responses (Ref 14, 15). Load, sliding speed and temperature are the independent parameters and CoF, A and SWR are the dependent parameters (responses) in this study. Since Incoloy 825 is exposed to temperatures between room temperature and 650 C in industrial usage areas, the same temperature range was taken as basis in this study (Ref 10, 11, 13). In addition, the parameters required for the formation of visible traces were determined with the pioneer tests and used in the experimental design. A brief information is given about the independent parameters as presented in Table 1.

Set values of the factors for experiments were determined by utilizing Central Composite Design (CCD). Experimental set values and corresponding response values are presented in Table 2. Statistical operations have been conducted by means of Design Expert™ commercial statistical software. Applied methodology and steps followed in this study is stated in Fig. 1.

2.2 Experimental

In this study Incoloy 825, theoretical chemical composition of which listed in Table 3, specimens were prepared in rectangular prism with dimensions 25 × 25 × 2,5 mm by using high-speed precision cutting device. Before the wear test the specimens were grinded to get surface quality $R_a < 0.20$ μm. The optical microscope image of Incoloy 825 alloy is shown in Fig. 2.

As seen in Fig. 2, the microstructure of Incoloy 825 alloy consists of equiaxed grains, parallel lines indicating twinning mechanisms within grains (Ref 16), and well-defined grain boundaries. In addition, some secondary phases are occasionally seen in the matrix. Kangazian et al. (2017) determined that these phases are TiN or TiCN, and even if high soaking temperatures are used, these phases do not dissolve easily during the annealing process and persist in the structure (Ref 17).

Load, sliding speed and temperature values for each experiment were determined by CCD. Then, the wear tests were performed by using a ball-on-disk type wear machine (Turkyus POD&HT&WT, Turkey) equipped with temperature-controlled cell. Wear track diameter and sliding distance were kept constant at 10 mm and 200 m, respectively, for all experiments. Al_2O_3 abrasive ball with 1428 HV_{10} hardness and 6.0 mm diameter were used as abrasive ball in the experiments because of its high temperature stability (Ref 7, 19).

Profile of the wear track was inspected at four sections on each specimen by means of 3D Hommelwerke T8000 GmbH Germany optical profilometer. Worn area during the experiment was determined by using profilometer images. Volume losses and special wear rate of the samples were calculated by using worn area. The specific wear rate (k) was estimated with Archard's wear law (Eq. 1), where V is the volume loss, L is the applied load and D is the total relative sliding distance as stated in the previous study (Ref 20, 21).

$$\text{SWR} = \frac{V}{L * D} \tag{Eq 1}$$

3. Results and Discussion

Set values of the sliding speed, load and temperature were obtained by CCD for each experiment and are listed in Table 2. Corresponding maximum contact pressure, maximum shear stress, and contact radius values are calculated by means of HertzWin software, which utilizes Hertzian stress equations to calculate contact parameters, according to these parameters and added in Table 2.

It is seen from Table 2 that maximum contact pressure, maximum shear stress, and contact radius values increase as the load increases. On the other hand, these values decrease with increase in the temperature. Reason for increase in the maximum contact pressure, maximum shear stress and contact radius is action of bigger force values with increasing load. On the other hand, resistance of the base material against the ball decreases in higher temperatures because Young modulus and Poisson ratio values of substrate decrease (Ref 22).

Table 1 Information summary about independent variables

Factor	Name	Units	Minimum	Maximum	Coded low	Coded high	Mean	Std. dev
A (s)	Speed	mm/s	150	250	-1 (170.27)	+ 1 (229.73)	200.00	25.21
B (L)	Load	N	5	20	-1 (8.04)	+ 1 (16.96)	12.50	3.78
C (T)	Temperature	Celsius	25	650	-1 (151.69)	+ 1 (523.31)	337.50	157.53

Table 2 Set values of independent variables used in the experiments

| Exp. No	Sliding speed, mm/s	Load, N	Temperature, °C	Max. contact pressure, GPa	Max. shear stress, MPa	Depth of max. shear stress, μm	Contact radius, μm
E1	229.73	16.96	523.31	1.145	360.2	40.06	84.10
E2	229.73	16.96	151.69	1.211	382.3	38.82	81.78
E3	250.00	12.50	337.50	1.063	336.2	35.51	74.93
E4	170.27	8.04	151.69	1.094	345.3	35.06	73.87
E5	200.00	5.00	337.50	0.783	247.7	26.17	55.21
E6	200.00	12.50	337.50	1.063	336.2	35.51	74.93
E7	170.27	16.96	523.31	1.145	360.2	40.06	84.10
E8	200.00	12.50	337.50	1.063	336.2	35.51	74.93
E9	200.00	12.50	650.00	1.022	317.0	36.93	76.40
E10	170.27	16.96	151.69	1.211	382.3	38.82	81.78
E11	200.00	20.00	337.50	1.243	393.2	41.53	87.64
E12	170.27	8.04	523.31	0.892	280.9	31.24	65.58
E13	200.00	12.50	337.50	1.063	336.2	35.51	74.93
E14	200.00	12.50	337.50	1.063	336.2	35.51	74.93
E15	200.00	12.50	337.50	1.063	336.2	35.51	74.93
E16	229.73	8.04	523.31	0.892	280.9	31.24	65.58
E17	200.00	12.50	25.00	1.110	350.5	34.80	73.34
E18	200.00	12.50	337.50	1.063	336.2	35.51	74.93
E19	229.73	8.04	151.69	0.944	298.1	30.27	63.77
E20	150.00	12.50	337.50	1.063	336.2	35.51	74.93
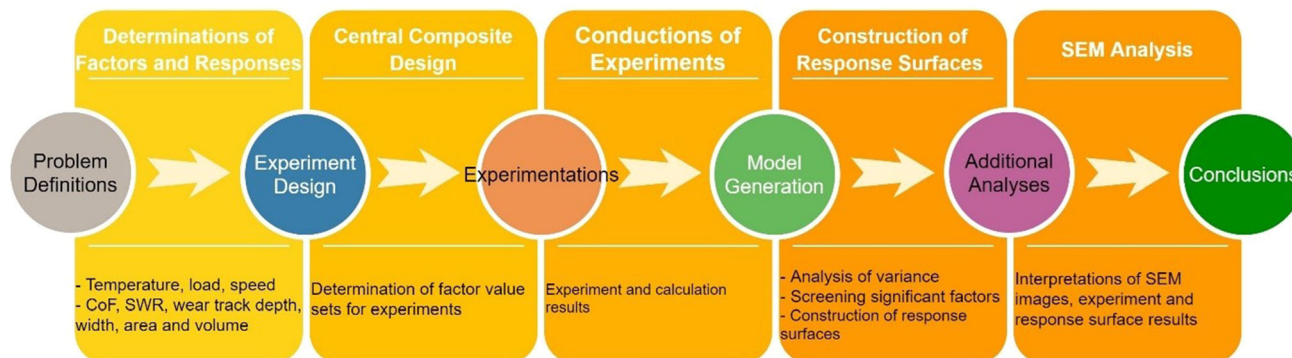
Fig. 1 Methodology and steps used in the study

Table 3 Theoretical chemical composition of Incoloy 825 (Ref 18)

Ni	Fe min	Cr	Mn	Mo	Ti	C	Nb	Si	Al	Impurities
40.18	30.32	22.6	0.67	2.88	0.94	0.008	0.025	0.26	0.1	Rest

Results of experiments conducted with independent parameter sets listed in Table 3 and regression model predictions corresponding to these parameters are presented in Table 4.

3.1 Statistical Results

Analyses of variances (ANOVA) were conducted to find the impact of factors on each response i.e., CoF, A, and SWR by using set values of the factors and results of the experiments.

3.1.1 CoF Model. Results of ANOVA studies for CoF are presented in Table 5. Degrees of freedoms (DF) in an ANOVA table indicate the measure of information involved in the data on the subject. The F value in the ANOVA table determines the ratio of explained variance to unexplained variance. If the model and term F values are greater than the critical F value in the 95% confidence interval then the model is significant. Significance of the model or considered term is also tested by p value. In hypothesis testing, p value is used to support or reject
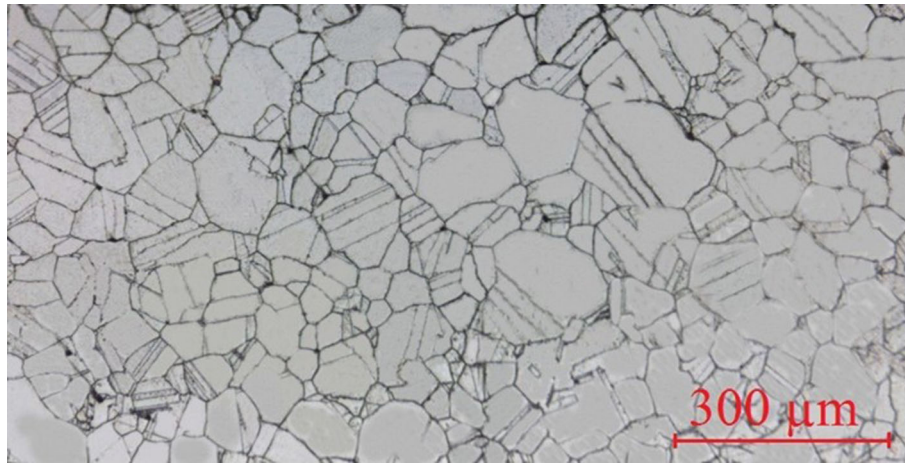
Fig. 2 OM microstructure view of Incoloy 825 Ni-CriFe superalloy

Table 4 Experiment results and predicted values of CoF, A and SWR obtained by regression models

| Exp. No | Coefficient of friction (CoF) | | Wear track area (A), μm^2 | | Specific wear rate (SWR), $mm^3/Nm \times 10^{-6}$ | |
	Actual value	Predicted value	Actual value	Predicted value	Actual value	Predicted value
E1	0.4890	0.485	11,750	11,132	108.77	81.18
E2	0.3055	0.234	11,946	11,328	110.59	83.00
E3	0.3283	0.345	11,308	12,182	142.02	181.04
E4	0.9010	0.793	3331	2713	65.04	37.45
E5	0.4352	0.496	3516	4390	110.4	149.42
E6	0.3812	0.318	9646	12,952	121.15	168.48
E7	0.4907	0.452	11,025	10,408	102.06	74.47
E8	0.3272	0.318	13,620	12,952	171.07	168.48
E9	0.3403	0.377	4365	7334	54.82	97.93
E10	0.4990	0.516	7695	7077	71.23	43.64
E11	0.3430	0.371	17,452	18,326	137.00	176.02
E12	0.3647	0.324	19,300	18,682	376.86	349.27
E13	0.2891	0.318	12,270	12,952	154.11	168.48
E14	0.3382	0.318	14,300	12,952	179.61	168.48
E15	0.3008	0.318	17,770	12,952	223.19	168.48
E16	0.3860	0.356	39,500	38,882	771.29	743.70
E17	0.5102	0.561	15,600	18,569	195.94	239.04
E18	0.2866	0.318	14,595	12,952	183.31	168.48
E19	0.4851	0.511	2235	1617	43.64	16.05
E20	0.4845	0.555	14,780	15,654	185.64	224.65

Table 5 ANOVA Results for CoF

Source	Sum of squares	DF	Mean square	F-value	p value	
Model	0.3254	8	0.0407	10.65	0.0003	Significant
s-Speed	0.0532	1	0.0532	13.93	0.0033	…
L-Load	0.0189	1	0.0189	4.94	0.0482	…
T-Temperature	0.0407	1	0.0407	10.67	0.0075	…
sT	0.0495	1	0.0495	12.95	0.0042	…
LT	0.0821	1	0.0821	21.51	0.0007	…
s^2	0.0316	1	0.0316	8.27	0.0151	…
L^2	0.0239	1	0.0239	6.25	0.0295	…
T^2	0.0412	1	0.0412	10.8	0.0073	…
Residual	0.042	11	0.0038	…	…	…
Lack of fit	0.0355	6	0.0059	4.5	0.0599	Not significant
Pure error	0.0066	5	0.0013	…	…	…
Cor total	0.3674	19	…	…	…	…

Table 6 Regression coefficients of CoF model in terms of coded and actual factor and rational impact of the terms on the response

Factor	Coefficient in terms of coded factors	Coefficient in terms of actual factors	% Effect on the response
Constant	0.318	5.03266	…
s (Speed)	-0.0624	-0.02809	13.13
L (Load)	-0.0372	-0.10076	7.83
T (Temperature)	-0.0546	-0.00572	11.49
sT	0.0786	0.000014	16.54
LT	0.1013	0.000122	21.32
s^2	0.0468	0.000053	9.85
L^2	0.0407	0.002046	8.57
T^2	0.0535	1.55E-06	11.26

the null hypothesis. This value is a proof that the null hypothesis is false. In general it is assumed that if the p value is smaller enough (less than 0.05 for the model and 0.1 for a term) then the model or term is supposed to have a significant effect on the response (Ref 23).

Reduced quadratic model in which the terms with p value of bigger than 0.1 are eliminated is developed for CoF. ANOVA results of CoF are listed in Table 5. Degree of freedom in the table is 8 which means the model constructed by using 8 terms. The Model F-value of 10.65 indicates that the model is significant, and the model p value of 0.0003 indicates that there is only a 0.03% chance that the F-value could occur due to noise. The model and terms s (speed), L (load), T (Temperature), sT, LT, s^2, L^2 and T^2 are significant because they have p values less than 0.1.

In Table 5, the ANOVA table created for CoF, it is seen that the speed is the most effective and the load is the least effective among the single parameters. In addition, considering the interactions of the parameters, it is seen that the $L*T$ interaction is the most effective term on the COF. In a study conducted on AISI 316L at constant temperature, it is seen that CoF is significantly affected by the interactions of load, sliding speed and sliding distance, on the other hand, floor*speed and distance*speed (Ref 21). Considering that the distance is constant and the temperature is variable in the current study, the differences are considered normal.

R-squared (R^2) is a statistical measure that quantifies the proportion of variation explained by an independent variable or variables in a regression model for a dependent variable. On the other hand, a high R^2 value does not always mean that the regression model is good. Because regardless of whether the variable is statistically significant, adding a new variable to the model always increases the R^2 value. So, in most statistical applications adjusted R^2 (R^2_{adj}) is used with or instead of R^2. To increase the accuracy of the model, the R^2_{adj} value increases when a necessary term is added, and when an unnecessary term is added this term decreases. In a good model, R^2 and R_{2adj} values are expected to be close to each other (Ref 24, 25).

CoF depends on various properties of the materials in contact, such as applied load, sliding speed, temperature, wear debris, etc. (Ref 26). CoF model has R^2 and R^2_{adj} values of 0.89 and 0.80, respectively. Since the R^2_{adj} is %80 of R^2 and R^2 is at an acceptable level the model is assumed to be adequate (Ref 27, 28).

Regression coefficients for CoF model in terms of coded and actual factors are listed in Table 5. The magnitude of the coefficients in terms of coded factors reflects the relative weight of that term in the regression model. It is seen from the table that the terms, s, L and T have negative effect on the CoF. On the other hand, the terms sT, LT, s^2, L and T^2 influence positively the response. Rational impact of the terms on the CoF is also presented on Table 6.

Developed regression model for CoF stated by using coefficients in terms of actual factors is formulated by Eq. 2. The predicted-against-actual-values graphs of the response variables in Fig. 3 depict the regression model's fit to the real experimental data. It can be seen in Fig. 3(a) that the graph's points are distributed uniformly and are close to the 45° line (Ref 18). This implies that the model aptly describes the real case.

$$\begin{aligned} CoF = {} & 5.03266 - 0.2809s - 0.10076L - 0.00572T \\ & + 0.000014sT + 0.000122LT + 0.000053s^2 \\ & + 0.002046L^2 + 0.00000155T^2 \end{aligned} \quad \text{(Eq 2)}$$

3.1.2 Average Wear Track Area. For the average wear track area, a reduced cubic regression model was created, and the ANOVA results are shown in Table 7. The model developed by using 12 terms. F-value and p value of the model are 10.67 and 0.0022, respectively. This indicates that the model is significant, with a 0.22 percent possibility of being this F value due to noise. The terms L (load), T (temperature), LT, sLT, s^2L, s^2T and sL^2 are significant in the model with p values of less than 0.1. The other terms i.e., s (speed), AB, AC, A^2, B^2 are insignificant and included in the model due to hierarchy.

In Table 7, it is seen that the parameter with the highest direct effect on the wear track area is the load, and $L*T$ and s^2T are quite effective in multiple interactions.

The R^2 and R^2_{adj} values for the area model are 0.95 and 0.85, respectively. The model is judged to be adequate because the R^2_{adj} is in the region of 80 percent of R^2 and R^2 is at an acceptable level (Ref 27, 28).

Table 8 shows the regression coefficients for the average track area model in terms of coded and real components. It is seen from the table that s, T, sL, LT, s^2, s^2T and sL^2 effect positively the area and the other terms (L, sT, L^2, sLT, s^2L) have negative effect on the response. The terms s^2T, s^2L, LT and L have biggest rational impact on the model with values of 23.56, 15.62, 14.20 and 9.40%, respectively.

Equation 3 is a developed regression model for area that is expressed using coefficients in terms of actual factors in Table 8. The graph's points are distributed uniformly and are close to the 45° line, as seen in Fig. 3(b). This means that the model accurately describes the real-world situation.

$$\begin{aligned} A = {} & -100156 + 179.514s - 37354.875L + 2210.782T \\ & + 557.164sL - 23.319sT + 17.632LT + 0.884s^2 \\ & - 1395.705L^2 - 0.126sLT - 1.747s^2L + 0.063s^2T \\ & + 6.837sL^2 \end{aligned}$$

$$\text{(Eq 3)}$$

3.1.3 Specific Wear Rate. For specific wear rate, a reduced cubic model was established. Table 9 shows the results of the ANOVA. Degree of freedom of the model is 12 and it is constructed by 12 terms. The model has an F-value of 12.27 and a p value of 0.0014, indicating that it is significant. The terms sT, LT, sLT, s^2L and s^2T, in the model show
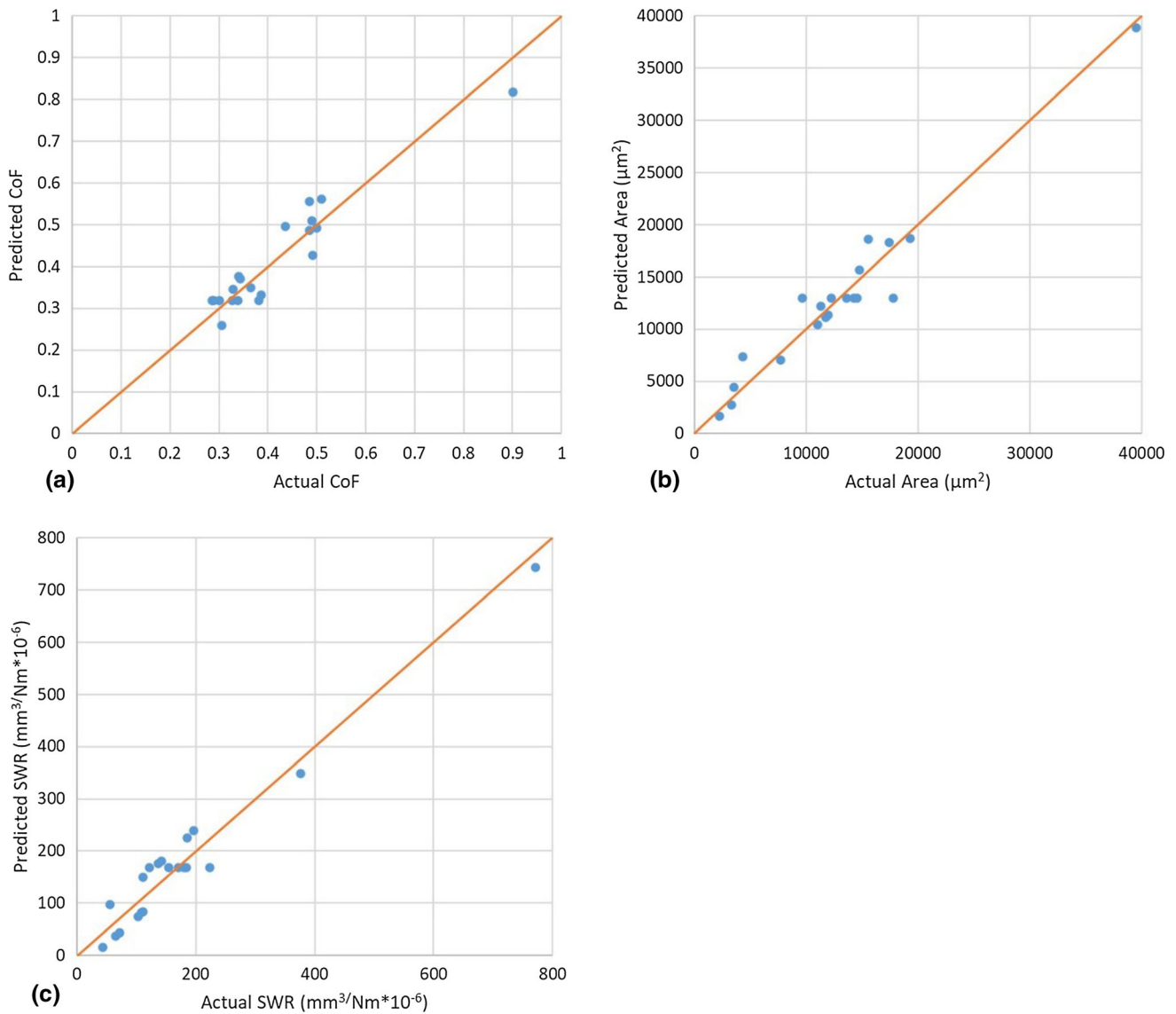
Fig. 3 Predicted vs. actual distribution for responses

significant p values less than 0.1. The terms s (speed), L (load), T (temperature), sL, s^2, L^2 and sL^2 are contained in the model because of hierarchy.

That S, L and T neither have a direct significant effect on SWR. However, it is seen that $L*T$, s^2L and s^2T have an effect on SWR, most notably in the form of interaction of factors. On the other hand, in the study on AISI 316L, it was reported that the load, speed and sliding distance and their cross-interactions were evident on SWR (Ref 21).

R^2 and R^2_{adj} for the SWR model are 0.95 and 0.88, respectively. The difference between R^2 and R^2_{adj} is less than 20% of the net amount, indicating that the model is acceptable (Ref 27, 28).

Regression coefficients of coded and actual factors are listed in Table 10. The terms effecting the SWR model in negative way are s, L, sT, L^2, sLT, s^2L and sL^2. On the other hand T, sL, LT, s^2, s^2T and sL^2 have positive effect on the response. The terms s^2T, LT and s^2L have biggest impact and the other terms have minor impact on the response.
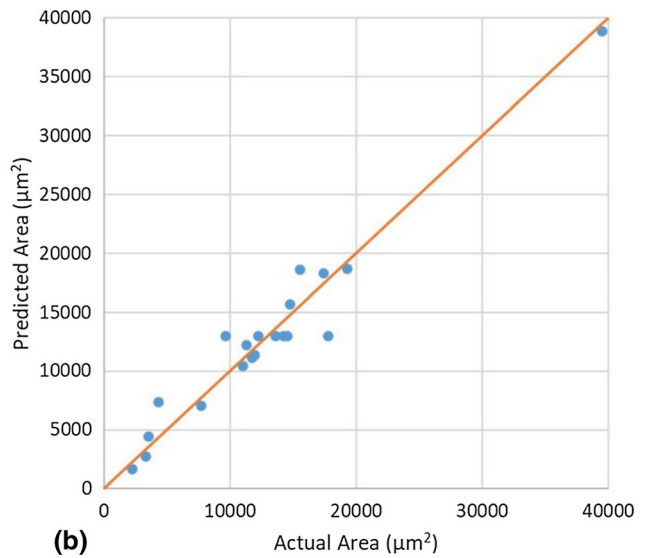
For the development of the regression equation of width, which is specified in Eq. 4, coefficients in terms of actual components are utilized. Actual versus predicted SWR values are shown in Fig. 3(c). In the vicinity of the 45° line, the points in the graph exhibit a relatively good distribution. This demonstrates that the regression model is a good fit for reality.

$$
\begin{aligned}
SWR = {} & -1240.29 - 0.1241s - 659.94L + 37T + 9.461\text{sL} \\
& - 0.39sT + 0.303\text{LT} + 0.021s^2 - 22.209L^2 \\
& - 0.0023\text{sLT} - 0.029s^2L + 0.0011s^2\text{T} + 0.111\text{sL}^2
\end{aligned}
$$

(Eq 4)

3.2 Discussions

Computer simulations are important in the wear event. Because it can provide an overview of the relationship between laboratory testing and computer simulations performed, and how the use of both, with all their limitations, can help explain the complex issue of microstructural changes in the wear phenomenon (Ref 29).

Table 7 ANOVA Results for track area

Source	Sum of squares	df	Mean square	F-value	p value	
Model	1.16E + 09	12	9.65E + 07	10.67	0.0022	Significant
s-Speed	6.03E + 06	1	6.03E + 06	0.6665	0.4412	…
L-Load	9.71E + 07	1	9.71E + 07	10.74	0.0135	…
T-Temperature	6.31E + 07	1	6.31E + 07	6.98	0.0333	…
sL	2.50E + 07	1	2.50E + 07	2.76	0.1407	…
sT	3.95E + 07	1	3.95E + 07	4.36	0.0751	…
LT	3.14E + 08	1	3.14E + 08	34.69	0.0006	…
s^2	1.70E + 06	1	1.70E + 06	0.1877	0.6779	…
L^2	4.62E + 06	1	4.62E + 06	0.5109	0.4979	…
sLT	7.70E + 07	1	7.70E + 07	8.51	0.0224	…
s^2L	1.57E + 08	1	1.57E + 08	17.38	0.0042	…
s^2T	3.58E + 08	1	3.58E + 08	39.52	0.0004	…
sL^2	5.42E + 07	1	5.42E + 07	5.99	0.0443	…
Residual	6.33E + 07	7	9.05E + 06	…	…	…
Lack of fit	2.71E + 07	2	1.36E + 07	1.87	0.2474	Not significant
Pure error	3.62E + 07	5	7.24E + 06	…	…	…
Cor total	1.22E + 09	19	–	…	…	…

Table 8 Regression coefficients of wear track area model in terms of coded and actual factor and rational impact of the terms on the response

Factor	Coefficient in terms of coded factors	Coefficient in terms of actual factors	% Effect on the response
Constant	12,951.73	− 100,156	…
s (Speed)	− 1032.33	179.514	2.34
L (Load)	4143.3	− 37,354.875	9.40
T (Temperature)	− 3340.19	2210.782	7.58
sL	− 1766	557.164	4.01
sT	2221.25	− 23.319	5.04
LT	− 6262.42	17.632	14.20
s^2	341.51	0.884	0.77
L^2	− 563.47	− 1395.705	1.28
sLT	− 3102.75	− 0.126	7.04
s^2L	− 6887.13	− 1.747	15.62
s^2T	10,386.27	0.063	23.56
sL^2	4042.33	6.837	9.17

Table 9 ANOVA Results for SWR

Source	Sum of squares	df	Mean square	F-value	p value	
Model	4.56E + 05	12	38,003.79	12.27	0.0014	Significant
A-Speed	951.03	1	951.03	0.307	0.5968	…
B-Load	353.74	1	353.74	0.1142	0.7453	…
C-Temperature	9956.24	1	9956.24	3.21	0.1161	…
AB	13,363.21	1	13,363.21	4.31	0.0764	…
AC	18,354.23	1	18,354.23	5.92	0.0451	…
BC	1.28E + 05	1	1.28E + 05	41.2	0.0004	…
A^2	2148.82	1	2148.82	0.6937	0.4324	…
B^2	60.4	1	60.4	0.0195	0.8929	…
ABC	25,140.87	1	25,140.87	8.12	0.0247	…
A^2B	44,534.82	1	44,534.82	14.38	0.0068	…
A^2C	1.02E + 05	1	1.02E + 05	32.95	0.0007	…
AB^2	14,152.8	1	14,152.8	4.57	0.0699	…
Residual	21,684.69	7	3097.81	…	…	…
Lack of Fit	15,972.1	2	7986.05	6.99	0.0356	Significant
Pure Error	5712.6	5	1142.52	…	…	…
Cor Total	4.78E + 05	19		…	…	…

Table 10 Regression coefficients of SWR model in terms of coded and actual factor and rational impact of the terms on the response

Factor	Coefficient in terms of coded factors	Coefficient in terms of actual factors	% Effect on the response
Constant	168.48	− 1240.29	…
s (Speed)	− 12.97	− 0.1241	1.84
L (Load)	7.91	− 659.94	1.12
T (Temperature)	− 41.95	37.0026	5.95
sL	− 40.87	9.4608	5.80
sT	47.9	− 0.3903	6.79
LT	− 126.31	0.3027	17.92
s^2	12.15	0.0207	1.72
L^2	− 2.04	− 22.2089	0.29
sLT	− 56.06	− 0.0023	7.95
s^2L	− 115.93	− 0.0294	16.45
s^2T	175.51	0.0011	24.90
sL^2	65.35	0.1105	9.27

3.2.1 Coefficient of Friction. CoF behavior of specimens against time under changing under different temperature, load and sliding speed conditions are plotted in Fig. 4(a), (b) and (c), respectively.

CoF behavior of specimens against time under changing under different temperature, load and sliding speed conditions are plotted in Fig. 4(a), (b) and (c), respectively. It seen in Fig. 4(a) that, increase in the temperature causes decrease in the CoF levels. This is because of an oxidation mechanism occurring in metallic materials owing to oxidation on the surface of the substrate subjected to dry sliding test under unlubricated conditions (Ref 29). This type of wear is known as oxidation wear and it is a result of reaction of ambient oxygen and metal surface (Ref 30). Oxidation on the surface mostly tends to decrease CoF but after some sliding time the oxide layer is broken and it effects CoF behavior conversely (Ref 31, 32). Even in experiment conducted at room temperature oxidation type wear can occur. Because temperature at contacting surface may rise dramatically due to interaction of load and speed at high values. At high temperatures elemental metal turns into metal oxides. Metallurgists are well aware that the hardness of metal oxides can be two or three times that of the metal itself (Ref 32). On the other hand, metal oxides have much lower heat and electrical conductivity (Ref 33) which may lead oxide layer change into more composite structure or change in the type of chemical compound.

In Fig. 4(b) CoF is decreased slightly as the load increases, but it is seen that the load is not significant on CoF as the temperature. This is because of instant increase in the temperature at sliding surface resulted from load and sliding speed and formation of oxides as mentioned above.

The variation of the friction coefficient depending on temperature and sliding speed for constant values of the load is shown in Fig. 5. In Fig. 5(a), it is seen that the friction coefficient increases sharply with the decrease in temperature in the region where the sliding speed is around 150 mm m/s for the 8 N value of the load. Similarly, in the region where the sliding speed is 250 mm/s, the friction coefficient shows a nearly horizontal change as the temperature decreases from 650 to 490 °C, but increases slightly as it decreases from 490 to 20 °C. On the other hand, while the speed decreases from 250 to 150 mm/s in room temperature region, the friction coefficient increases rapidly. In the region where the temperature is 650 °C CoF decreases slightly while the speed increases from 150 to 200 mm/s but it increases slowly as the speed increases from 200 to 250 mm/s. When Fig. 5(b) and (c) is examined, in cases where the load is 12.5 N and 17 N, the highest friction coefficient is occurring at room temperature with the sliding speed of 150 mm/s. However, CoF decreases as the load increases in these graphs. Again, it can be deduced from these two graphs that the effect of temperature and sliding speed on the friction coefficient decreases as the load increases (Ref 34). In addition, as the load increases, it is seen that the friction coefficient tends to increase in the region where the temperature and sliding speed are high. It is understood from Fig. 5(a), (b), and (c) that load is an effective parameter on CoF. At high sliding speed values decrease in the CoF continues up to 498 °C under 8 N load but under 12.5 N load, negative trend continues up to 355 °C. Moreover, the trend changes into increase between 20 and 650 °C under 17 N load. These CoF behaviors imply that glazed layer occurred by increased temperature is broken as the load increases.

Figure 6 depicts the CoF response surface at constant temperature of 150, 340 and 600 °C depending on the load and shear rate. In Fig. 6(a) which is plotted for the constant value of 150 °C, maximum CoF occurs in the region of 5 N load and 150 mm/s sliding speed. CoF is decreasing parabolically from this point to 20 N load and 250 mm/s sliding speed point. It is seen in Fig. 6(b) that significance of the load and the sliding speed decreases substantially at 340 °C. When the temperature exceeds 600 °C, as seen in Fig. 6(c), the effect of load and speed on CoF reverses, compared to 150 °C. In other words, maximum CoF region at 600 °C corresponds 20 N load and 250 mm/s speed point (Fig. 6c).

The oxidation and the associated COF values due to the chemical reaction even at room temperature were evaluated before. At high temperatures, oxide formation is accelerated on the surfaces of metallic materials (Ref 31). In addition, the oxide thickness formed on the surface also increases. One of the most important reasons for this is that both metal and oxygen atoms can move faster at high temperatures (35). After a certain degree of the temperature, oxidation wear starts to change into corrosion type wear and this occasion is a cause of increase in the wear volume losses. In addition, rapid oxidation at high temperatures forms the basis of oxidation type wear (Ref 23). The thickness of oxide layer and the roughness on the surface caused by its shedding increase the COF value. Moreover, piercing of these abrasion wastes between the interacting surfaces will cause additional increase in the COF value.

3.2.2 Wear Track Area. The 3-dimensional view of the wear track images of some samples is given in Figs. 7 and 8 shows the variation of wear track area response surface with sliding speed and temperature under constant load of 8, 12.5 and 17 N. In Fig. 8(a), it can be seen that in the region where the temperature is 160 °C under 8 N load, the trace area almost does not change with the sliding speed and remains around 3500 μm^2. With increasing temperature, the track area grows linearly for speeds between 160 and 230 mm/s. The slope of the increase here is not constant, it reaches its lowest value at 200 mm/s and increases with both decrease and increase in speed. The track area changes in a parabolic way depending on
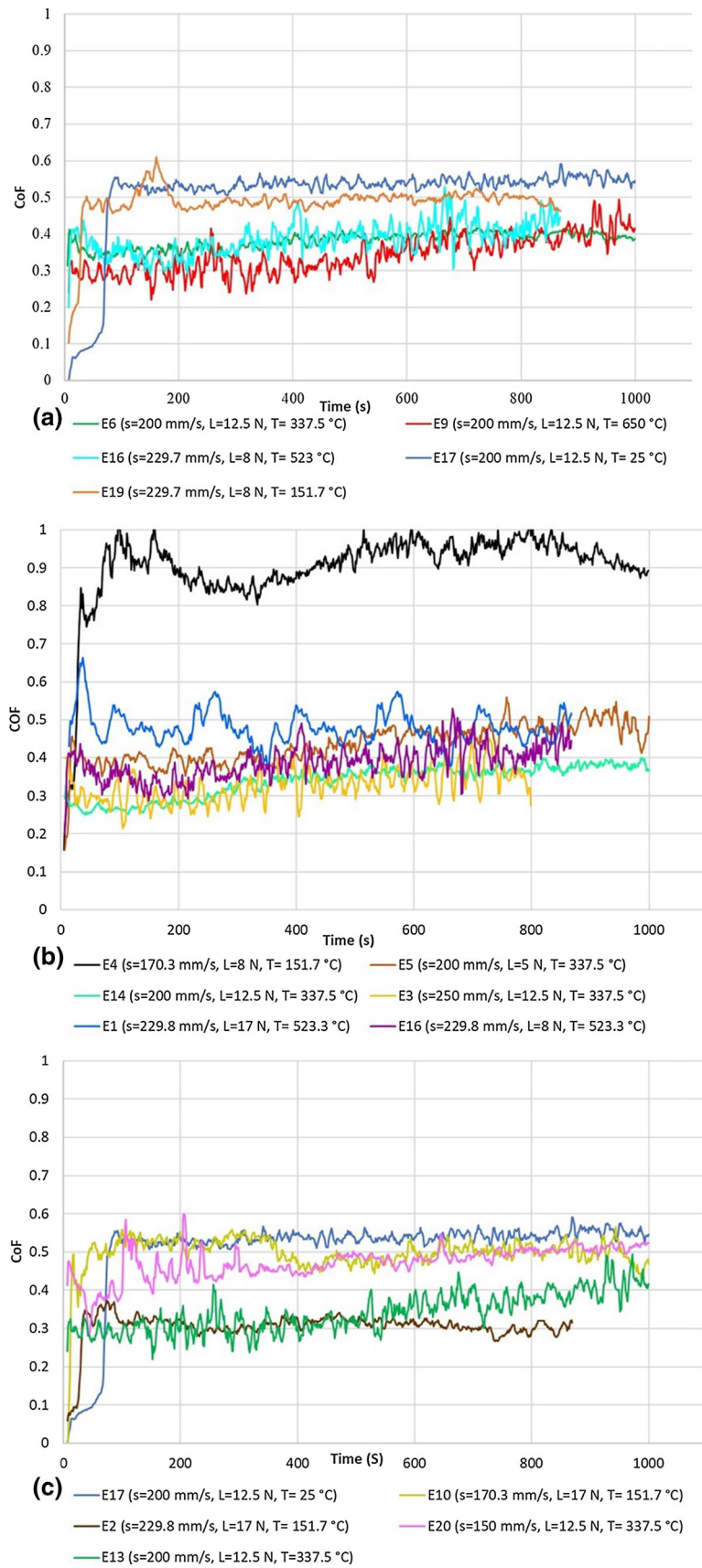
Fig. 4 Change in coefficient of friction according to (a) temperature, (b) load, (c) speed (experimental values)
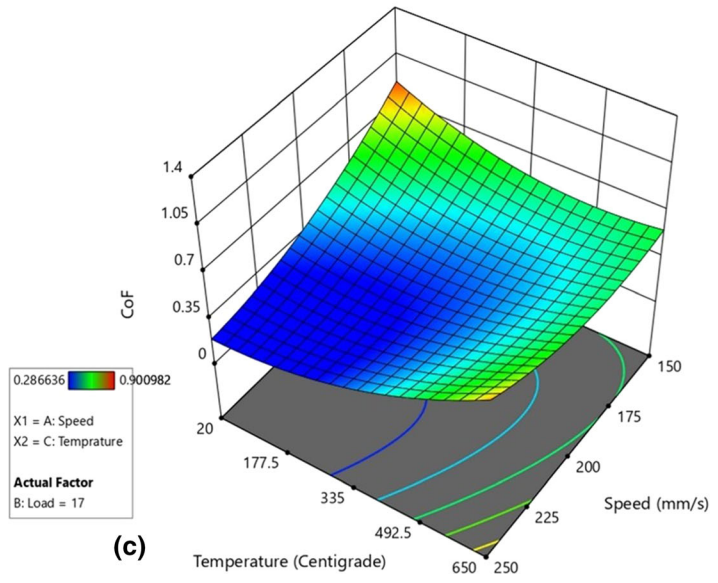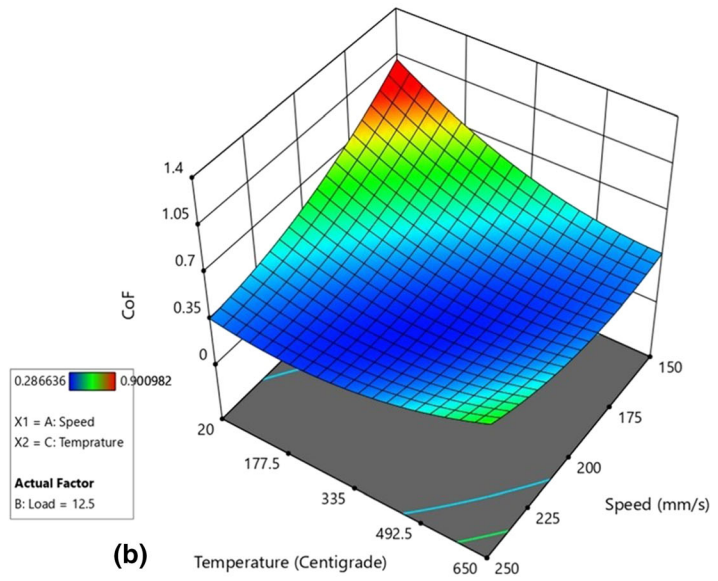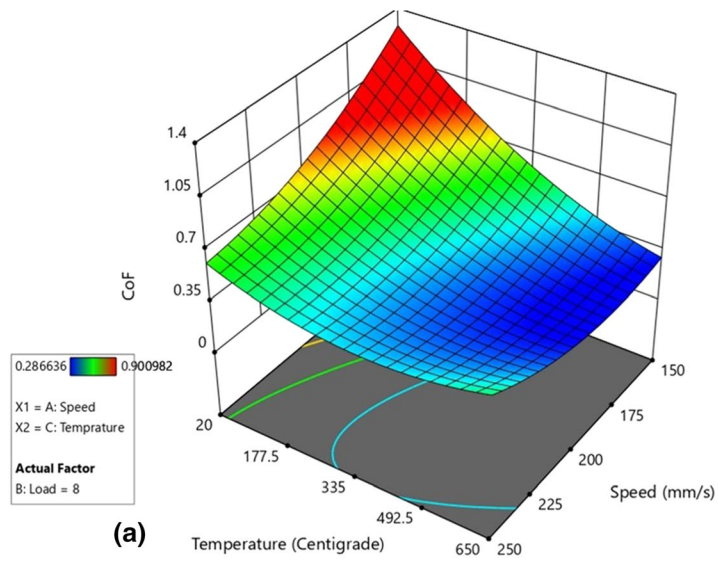
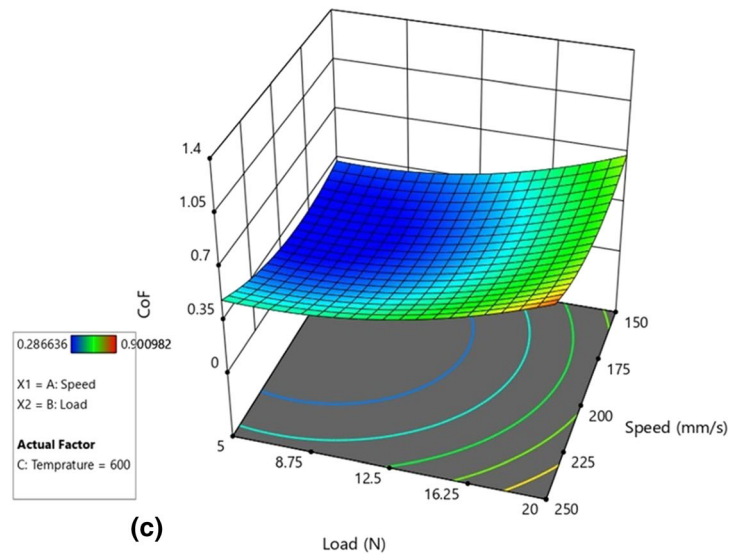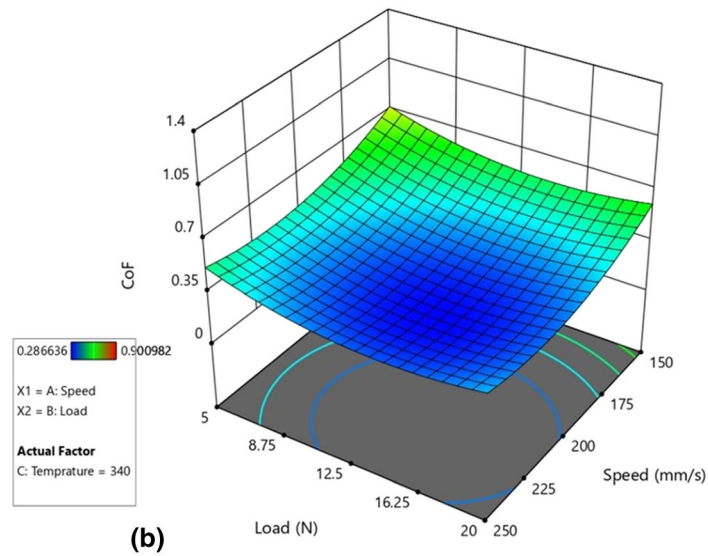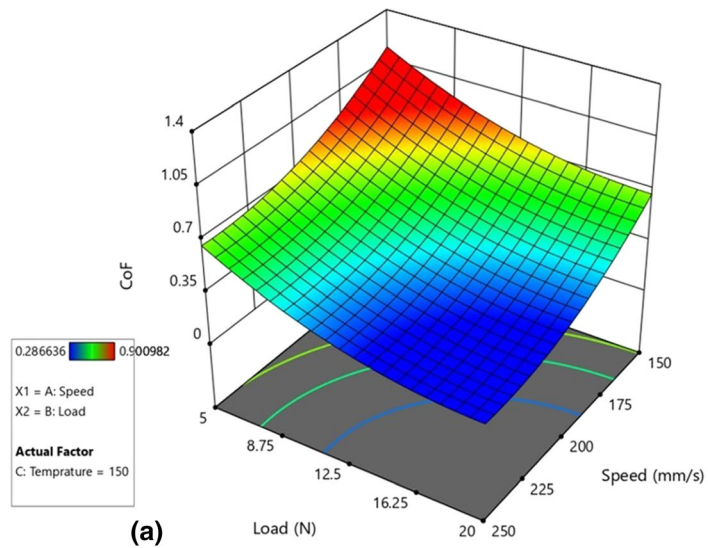**Fig. 5** Response surface for CoF for constant value of load at (a) 8 N, (b) 12.5 N (c) 17 N

Fig. 6 Response surface for CoF for constant value of temperature at (a) 150 °C, (b) 340 °C (c) 600 °C
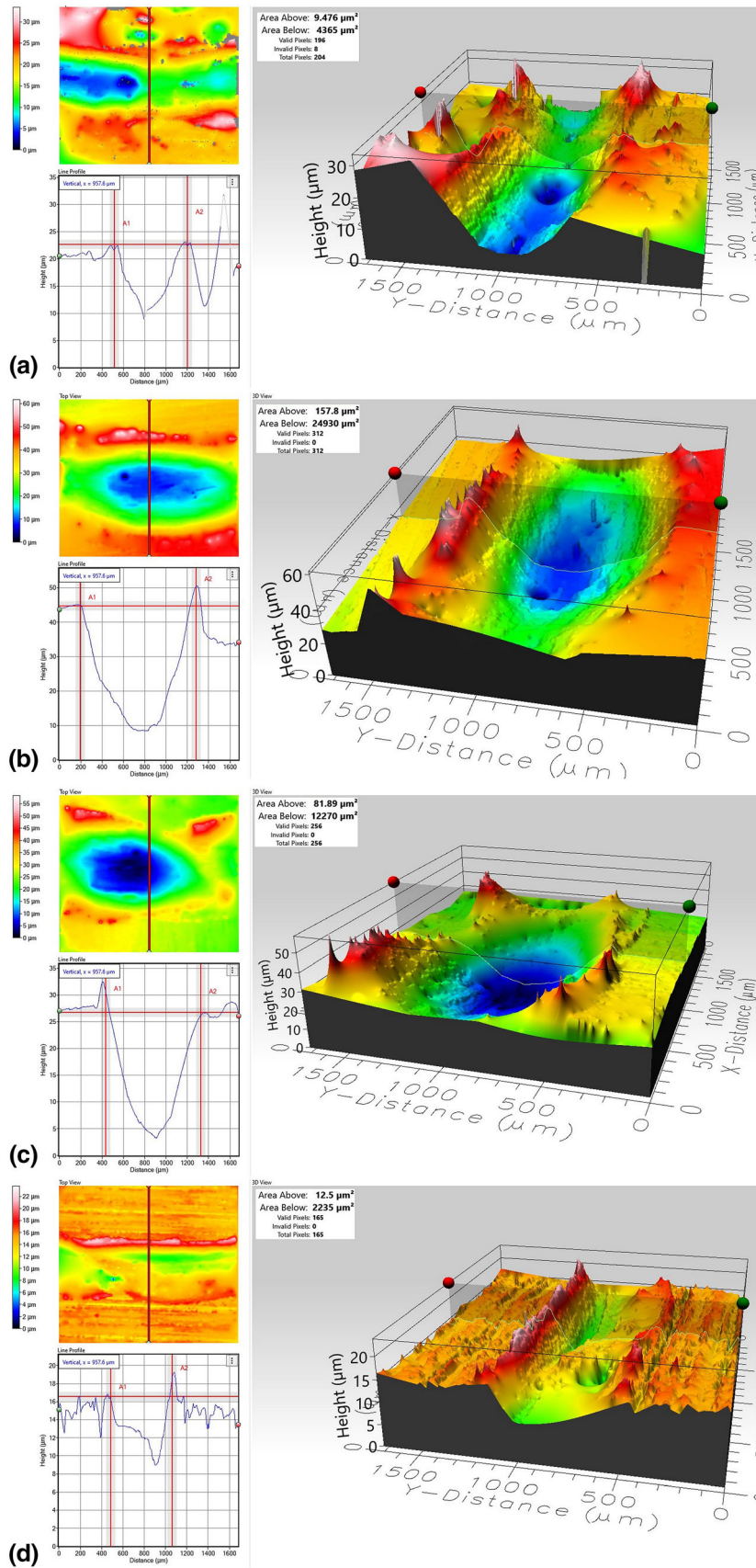
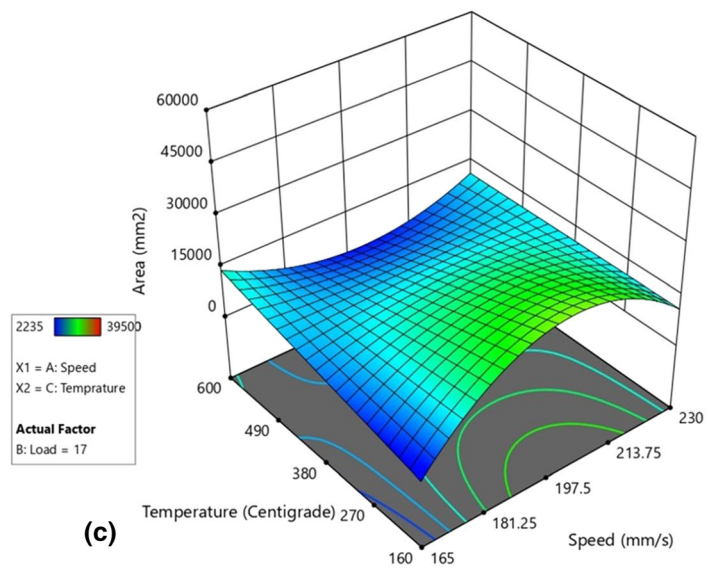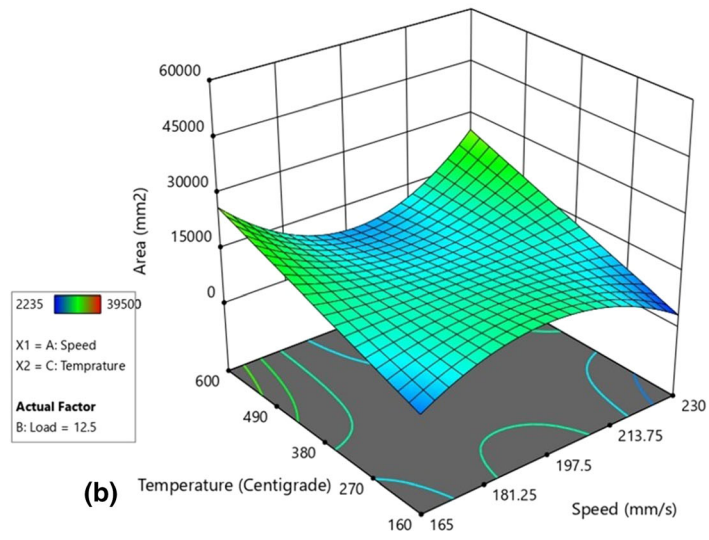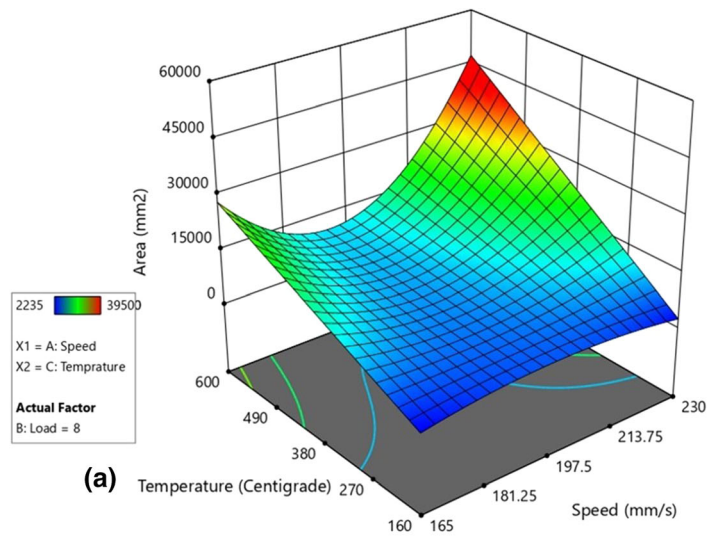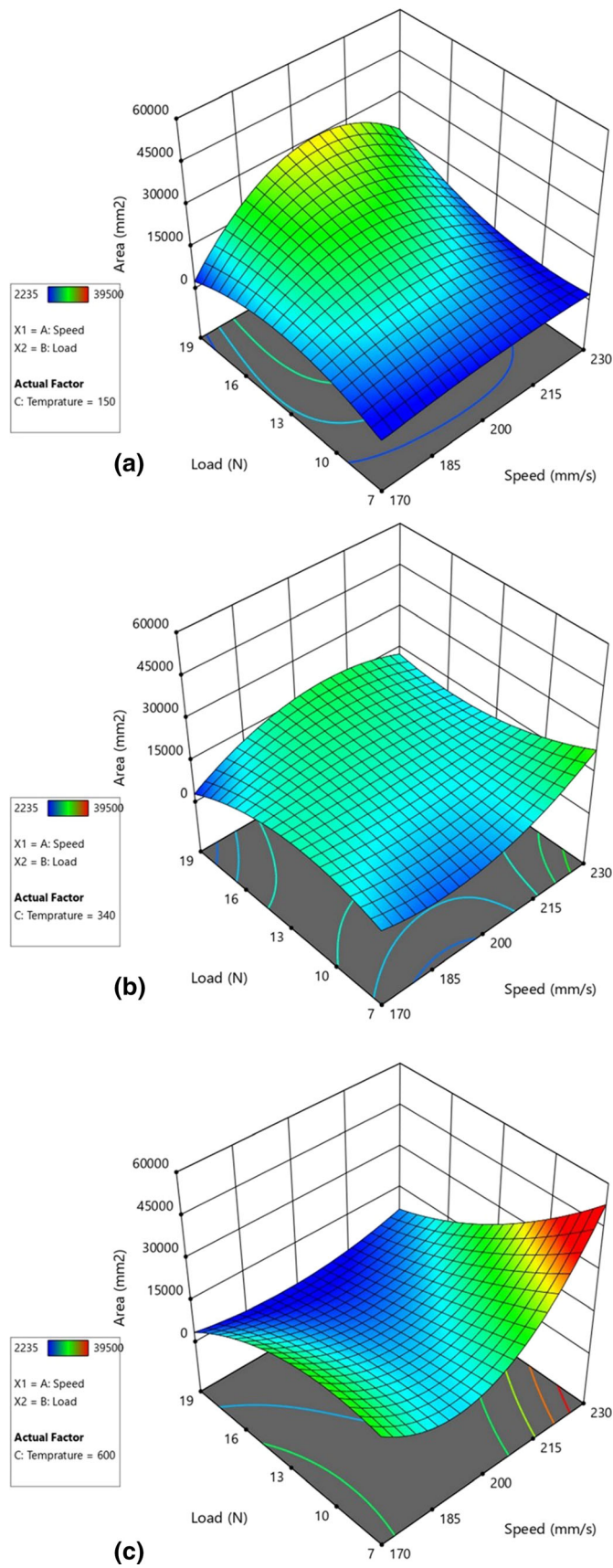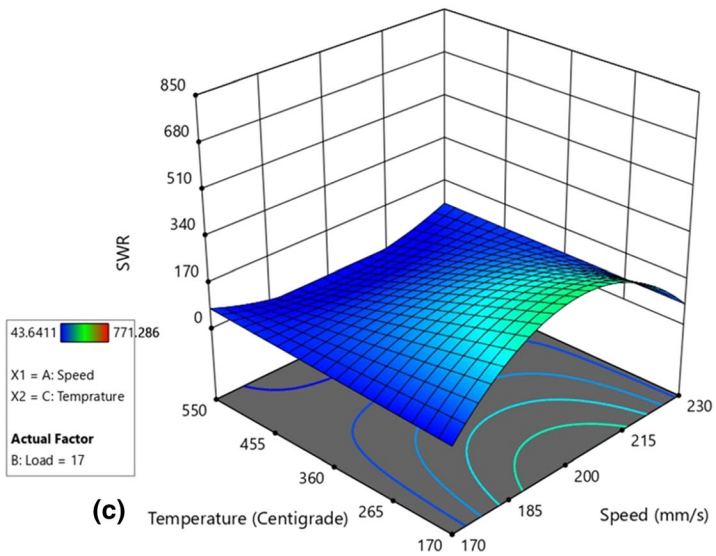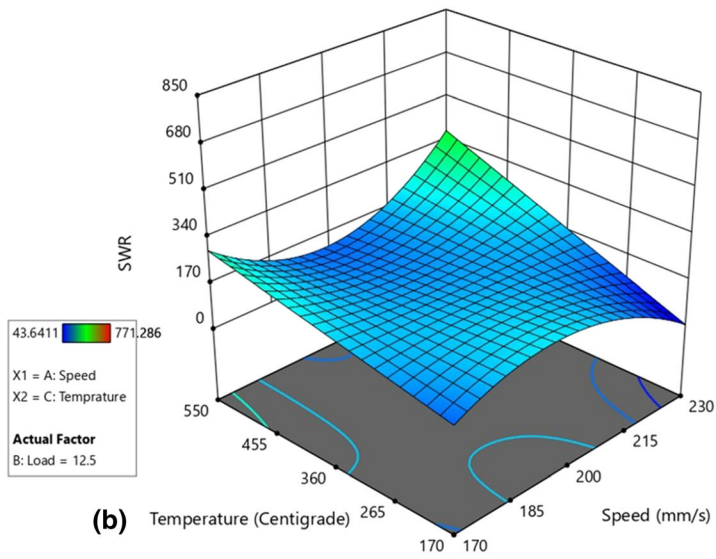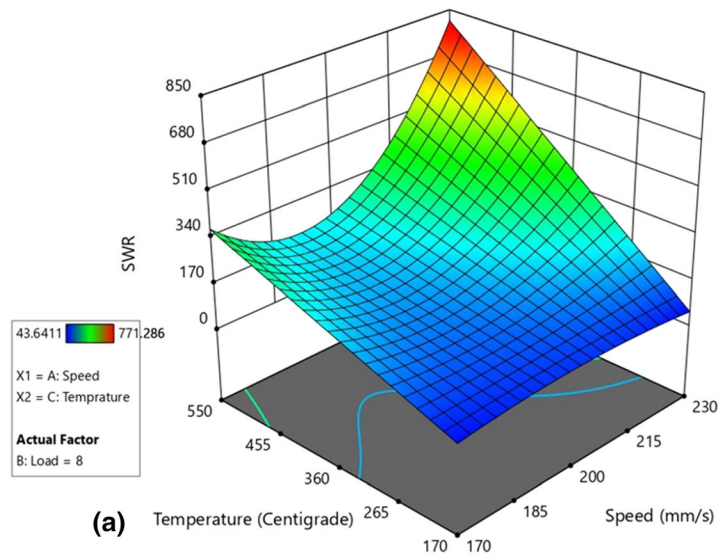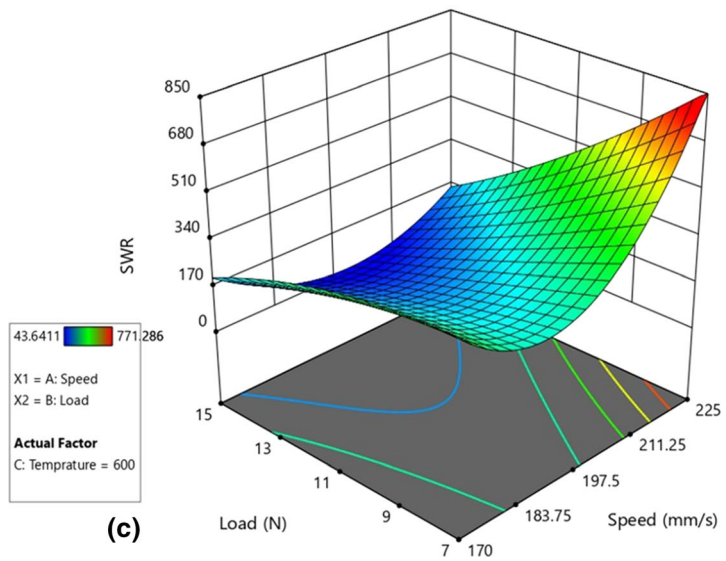**Fig. 7** Optical profilometer images and measurements of wear tracks for (a) E 9, (b) E 11, (c) E 13 (d) E 19

Fig. 8 Response surface for wear track area for constant value of load at (a) 8 N, (b) 12.5 N (c) 17 N

Fig. 9 Response surface for wear track area for constant value of temperature at (a) 150° C, (b) 340° C (c) 600° C

Fig. 10 Response surface for SWR for constant value of load at (a) 8 N, (b) 12.5 N (c) 17 N
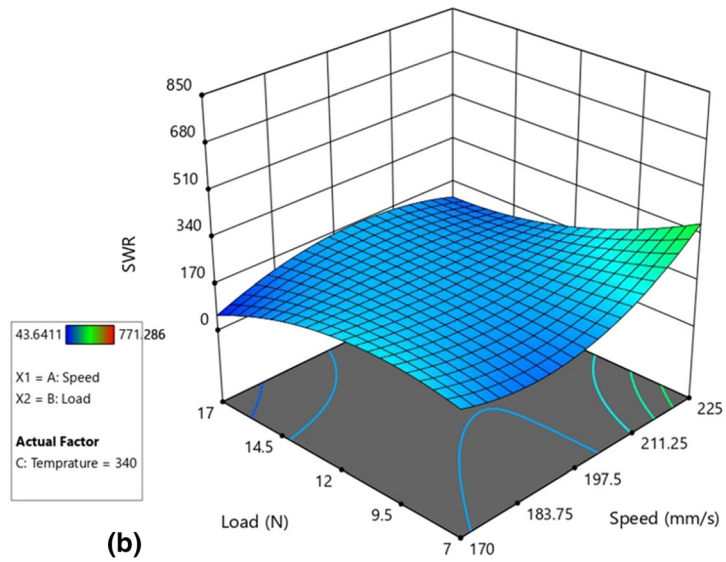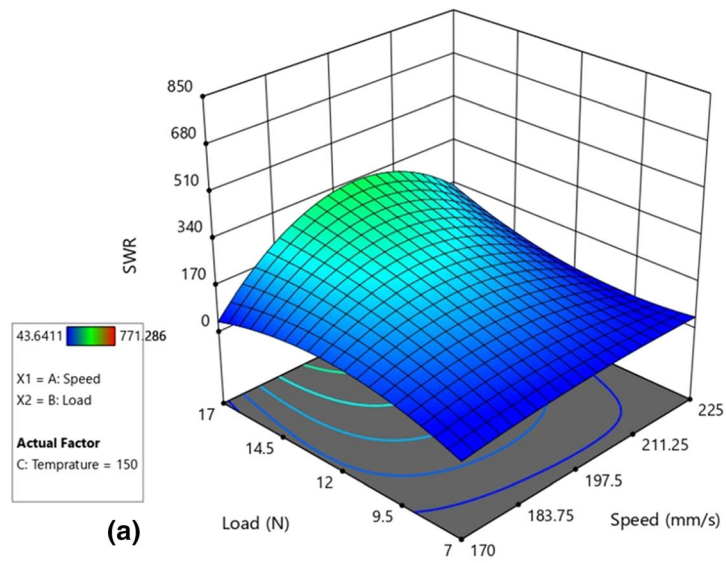
Fig. 11 Response surface for SWR for constant value of temperature at **(a)** 150° C, **(b)** 340° C **(c)** 600° C
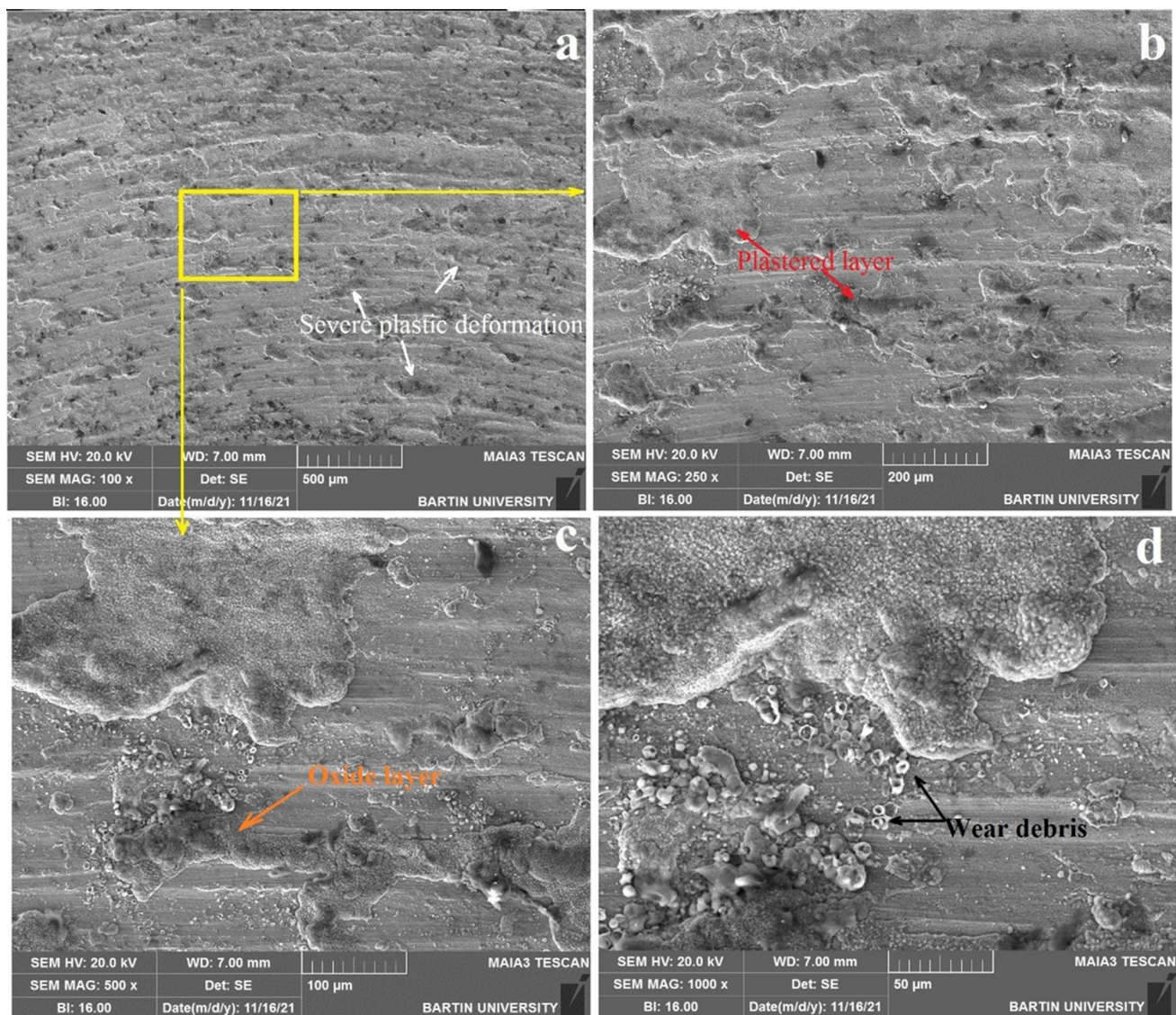
Fig. 12 Worn surface SEM micrograph of E17 (s = 200 mm/s, L = 12.5 N T = 25 °C) experiment sample **(a)** 100x **(b)** 250x **(c)** 500x **(d)** 1000x

the speed in the zone where the temperature is 600 °C, with the lowest value of the area occurring at 190 mm/s sliding speed. The highest track area value is 47000 μm^2 in the region where the temperature is 600 °C and the speed is 230 mm/s. When examining Fig. 8(b) and (c) together, it can be seen that as the load increases, the effects of temperature and speed on the track area decrease. The track area values range from 600 to 26,500 μm^2 under 12.5 N load and 200 to 26,000 μm^2 under 17 N load. The track area grows at low temperatures, especially at medium speeds, and is negatively influenced by speed increases or decreases, as shown in these two graphs. At high temperatures, the effect of sliding speed on the track area is observed to be reduced.

This situation can be approached from a variety of perspectives. First and foremost, as previously indicated, as the temperatures get higher, the wear mechanism transforms into corrosive wear (Ref 36). Another factor is that with the increase in temperature, the layer that is broken will be high. Plastic deformation feature of the regions that have not yet been oxidized or the oxide as a result, the likelihood of the metallic

surface sticking (adhesion) to the opposite surface will increase. As a result, oxidation, delamination, and adhesion forces will wreak havoc on the material. Furthermore, the abrasion effect of oxide compounds removed from the surface will contribute to the sample's abrasion.

Change in response surface of wear track area related to load and speed for at constant temperatures of 150, 340 and 600 °C. Track area does not change significantly with change in speed under load values at 150 °C. On the contrary under 19 N load it changes in inverse parabolic manner with a maximum point at 200 mm/s. It is seen from the plot that wear track area tends to increase with increasing load. Slope of the increasing trends is higher at mid-speed values (around 200 mm/s) with respect to lower and higher speeds. Effect of load and sliding speed on wear track area is decreasing relatively at 340 °C and the area value is fluctuating between 5900 and 23,500 μm^2. At constant temperature of 600 °C (in Fig. 9c) for 7 N load value, the area increases parabolically via 170 and 230 mm/s, with a base point at 190 mm/s. On the other hand, the area value is changing slightly around 3000 mm^2 under 19 N load. In the
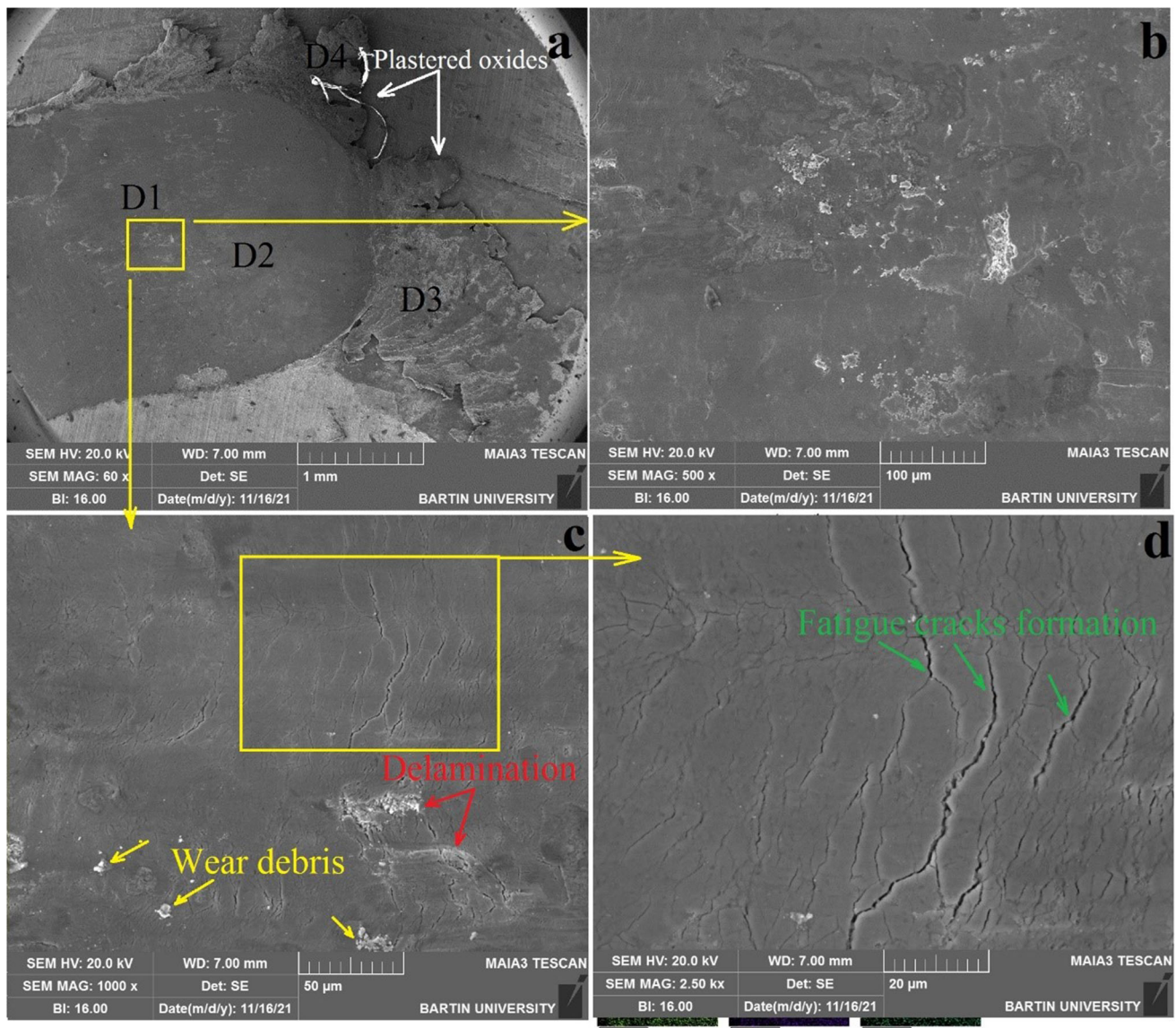
Fig. 13 Worn surface SEM micrograph of E9 (s = 200 mm/s, L = 12.5 N, T = 650 °C) experiment sample (a) 60x (b) 500x (c) 1000x (d) 2500x

region where the velocity is 170 mm/s, the area decreases toward 7 and 19 N in an inverse parabolic manner, with a peak point of 10 N. On the other hand, as the load decreases from 19 to 7 N at a velocity of 230 mm/s, the area increases parabolically.

3.2.3 Specific Wear Rate. The variation of the SWR response surface under constant loads of 8, 12.5 and 17 N, depending on sliding speed and temperature is presented in Fig. 10. SWR has its lowest value under 8 N constant load and low temperatures in Fig. 10(a). Glazed layer due to heat dissipation because of relative speed of wearing tip on the material is not broken at low speed and low temperature values so that SWR is relatively low in mentioned conditions.

However, when the temperature increased to 550 °C, the SWR increases parabolically toward the values of 170 and 230 mm/s, taking the lowest value in the region where the velocity is 190 mm/s. In the studied region, SWR got its highest value at 800, at the combination of the highest temperature (550 °C) and speed (230 mm/s). SWR generally

increases linearly with temperature, provided the speed remains constant. The slope of this rise increases as it approaches 230 mm/s. In most metallic materials, if the ambient temperature increases, the time required for the formation of a compact and protective oxide layer decreases (Ref 37). Fine metallic wastes broken at high temperatures stay on the wear surface, oxidize and become compact and form a glaze layer. They even cause a change in the wear mechanism. The wear particles formed during the interaction deform immediately afterward. In this way, a continuous source (clean surface) is created so that atmospheric oxygen can form the oxidation mechanism.

Figure 10(b) shows that under 12.5 N of load, the effect of temperature and sliding speed on SWR is relatively reduced. In regions where the speed is low and high such as 170 and 230 mm/s, SWR increases linearly with temperature, while it remains almost constant in the region where the speed is 200 mm/s. The highest SWR value occurs at a temperature of 400-550 °C and a speed of 230 mm/s. In Fig. 10(c), it is seen
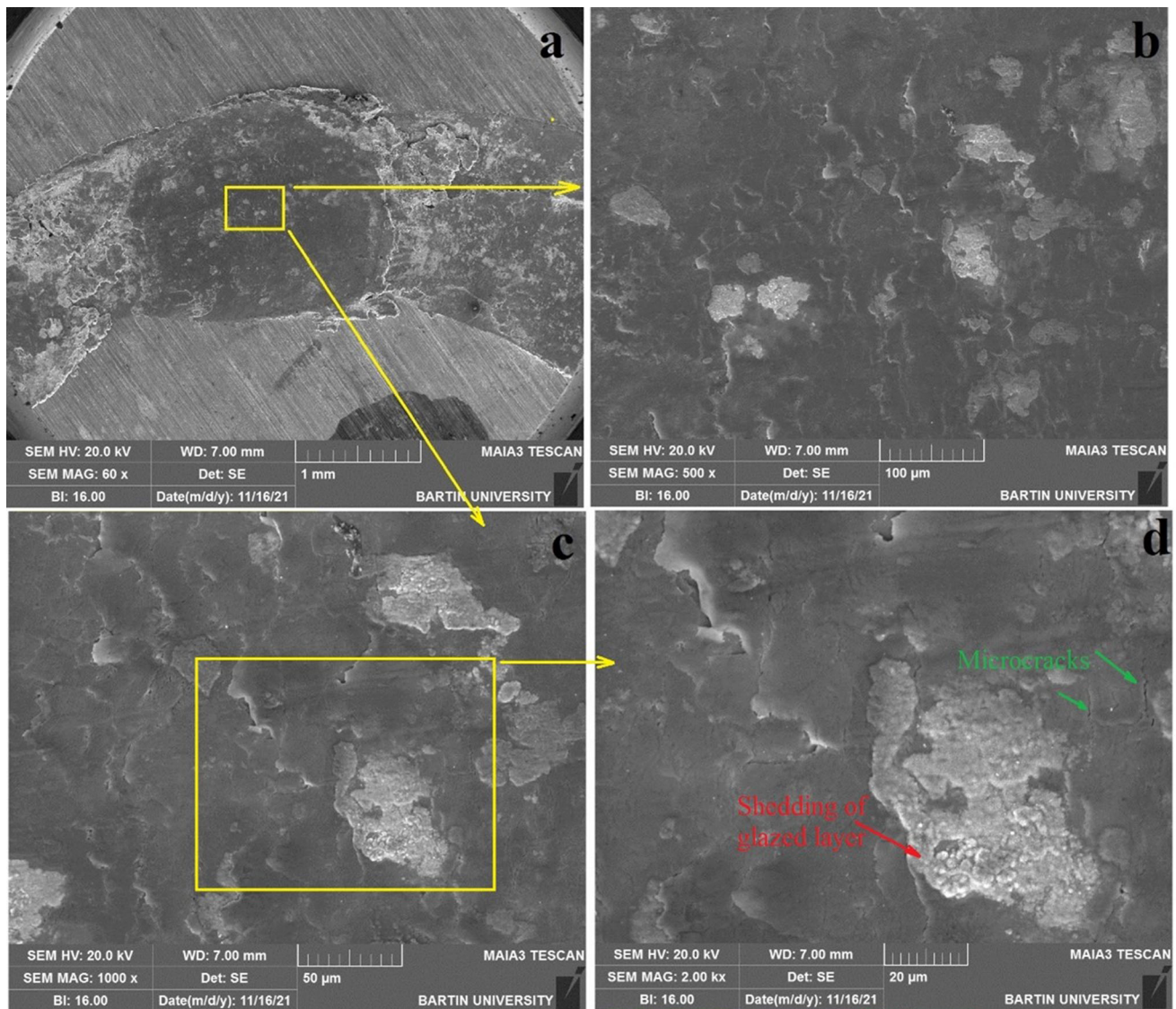
Fig. 14 Worn surface SEM micrograph of E16 (s = 229 mm/s, L = 8 N T = 523 °C) experiment sample (a) 60x (b) 500x (c) 1000x (d) 2000x

that the SWR at 17 N of the load remains constant for almost all temperature and speed values. Only in the overlap zone of 170 and 200 mm/s speed SWR increased slightly.

Variations of the SWR response surface at 150, 340, and 600 °C depending on load and sliding speed are presented in Fig. 11(a), (b), and (c), respectively. In Fig. 11(a), under 7 N load at 170 °C, SWR takes the value 170 regardless of speed. When the load increases to 17 N, the SWR decreases in inverse parabolic manner toward 170 and 225 mm/s velocities, with a peak in the 200 mm/s region of the speed. While SWR almost does not change with the load at low and high values of speed, it increases linearly with increasing load, with an increasing slope as the speed approaches 200 mm/s. Here, it is possible to say that the sliding speed of is the most effective parameter and a turning point in oxide formation and breaking is 197.5 mm/s.

When the temperature rises to 340 °C (Fig. 11b), SWR increases parabolically as the load decreases and the speed increases with the maximum point at load of 7 N and sliding speed of 225 mm/s. On the other hand SWR decreases with inverse parabolic path as the load increases from 7 to 17 N and the sliding speed decreases from 225 to 170 mm/s. However, at

this temperature level, the variation of SWR depending on load and speed is lower than at higher temperatures. The increase in temperature caused the sliding speed to have the opposite effect on the SWR than seen in the previous graph. Both decrease and increase around 197.5 mm/s in the sliding speed caused SWR to increase. Here, the fact that SWR is high at both low and high speeds is related with the rate of formation of the oxide layers formed on the surface, their thickening, breakage and the abrasion effect on the surface.

In Fig. 11(c), at 600 °C, SWR changes inversely proportional to the load at all speed values, but it is seen that the rate of this change is significantly higher at high speeds. It is seen that at low loads, SWR changes parabolic with the lowest value at the point where the speed is 185 mm/s, and the highest SWR value is at 7 N load and 225 mm/s speed. Aside from the oxidation caused by the high temperature, the thermal softening that will occur on the material surface (Ref 38, 39), as well as the thermal stresses that will occur due to the chemical composition difference between the oxidized surface and the substrate, have caused the SWR behavior to differ from that at lower temperatures.
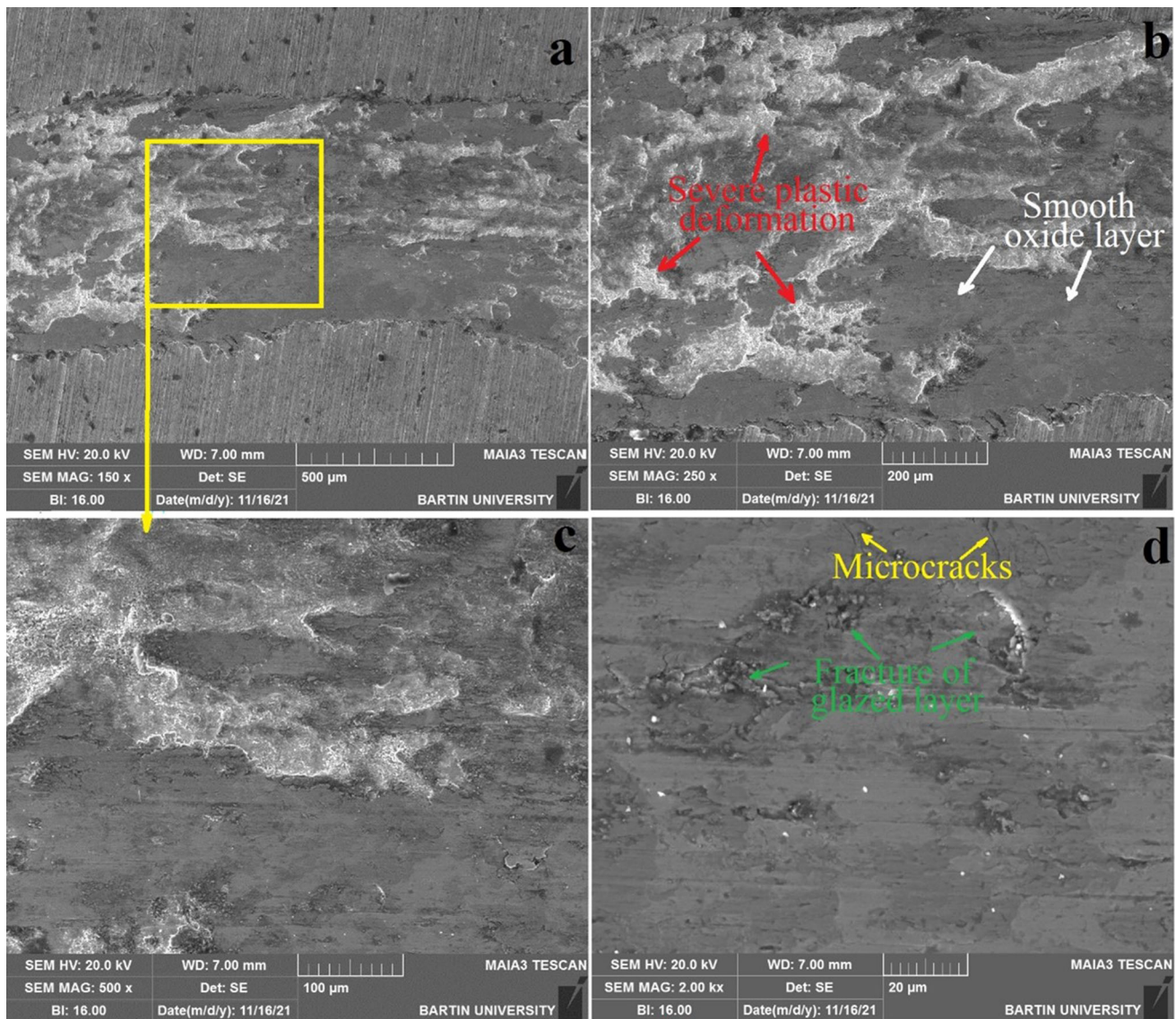
Fig. 15 Worn surface SEM micrograph of E19 (s = 229 mm/s, L = 8 N T = 151 °C) experiment sample (**a**) 150x (**b**) 250x (**c**) 500x (**d**) 2000x

3.2.4 Wear Modes and Mechanisms. SEM images of the sample surface subjected to the dry sliding wear test according to the E17 variable set in Table 2 are shown in Fig. 12. Severe plastic deformation, a plastered smooth layer and a surface made from wear debris are seen in the SEM views. Additionally, the presence of some oxidized areas, which are seen as dark gray in the picture, can be noticed. The presence of regions with high oxide content is clearly seen in the microstructure picture of the worn surface of this sample, which is given as supplementary Figure I.

It is seen in Fig. 13 that in SEM images of worn area E9, which is conducted with same sliding speed and load conditions as E17 but at 650 °C, wear mechanism is changed completely and it is turned into oxidation type mechanism. For a better understanding of the event, first of all, when the SEM view given at 60 × is examined, the regions indicated by D1 and D2 are the surfaces that are completely oxidized and come into contact with the abrasive ball. Debris in area D3 are generated in the wear direction and those in area D4 are debris pushed out of the wear path. The formation of the regions can be explained as follows. First of all, the regions designated D1 and D2 are the zones that, as previously said, are in direct contact with the abrasive ball. It is stated by many researchers that an oxide film forms on the surface during the interaction of the metallic material, even at room temperature (Ref 30-32, 40). In metallic materials, the development of oxide on the surface accelerates as the temperature rises (Ref 40). Many factors influence the production of oxide on the surface, ranging from the chemical structure of the sample to the shear rate and applied force. It's even capable of altering the oxide type. In this sample as well, a similar condition was seen. Because, as observed in the EDS mapping study, the oxide generated on the surface is noticeable both in color and structure when compared to the preceding sample (room temperature). In Fig. 13(c), in the part indicated by the yellow frame, the image of the region numbered D1 at 2500 × is given in Fig. 13(d). It is better understood how the oxide layer formed here, under cyclic loads, thin cracks are formed over time and these cracks combine with each other and cause damage, and thus, how it deteriorates with the fatigue type wear mechanism. First, by
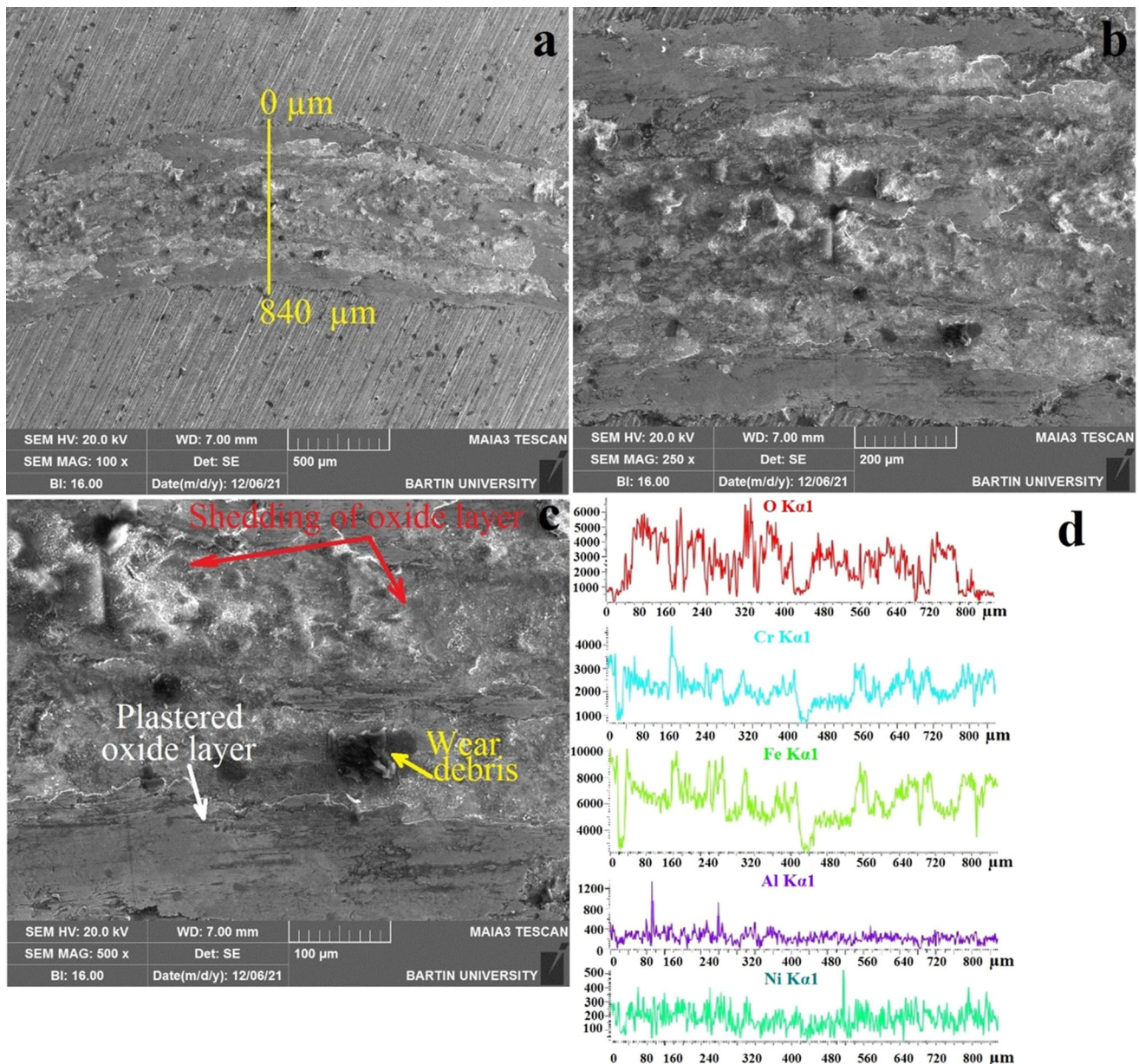
Fig. 16 Worn surface SEM micrograph of E4 (s = 170 mm/s, L = 8 N, T = 151 °C) experiment sample. μm

generating a glazing layer between the abrasive and the main material, this oxide layer, which is developed because of speed, load, temperature, and material structure, works as a solid lubricant (Ref 41-43). This layer begins to deteriorate over time, depending on the thickness and structure of the oxide layer formed on the surface. When Fig. 13(c) (area in yellow square) is examined, it is seen that the deterioration generally starts with microcracks perpendicular to the wear direction and secondarily parallel to the wear direction. This oxide layer (glazed layer), which is formed due to different test parameters, prevents metal-to-metal interaction between the interacting surfaces, causing the wear mechanism to change and the wear rate to decrease (Ref 40, 43-45). As a matter of fact, as seen in supplementary Figure II, high temperature caused the wear to have a nearly homogeneous oxide appearance everywhere.

When EDS mapping and SEM images of worn region of E16 (s = 229 mm/s, L = 8 N, T = 523 °C) sample are exam-

ined by Fig. 14, it is clear that oxidation type of wear prevails and oxidation is separated all around worn area as shown in Fig. 13. However, it is seen that the oxide layer formed on the surface contains fewer cracks than E9 and accordingly less shedding occurs. This is a result of the wear process being carried out with a lower load and lower temperature. As seen in supplementary Figure III, the parts in the form of white islets on the surface are composed of high rates of Fe and O_2, while the other parts exhibit a homogeneous distribution of other elements, in addition to the presence of high O_2.

When the SEM photograph (Fig. 15) taken from the wear track surface of E19 (s = 229 mm/s, L = 8 N, T = 151 °C) sample is examined, an excessive plastic deformation, a smooth layer and a surface formed by wear debris are seen, similar to the surface view of Fig. 12. As can be seen in Fig. 15(d), it is seen that the damage mechanism occurs as a result of fracture of microcracks formed in the oxide regions. As seen in
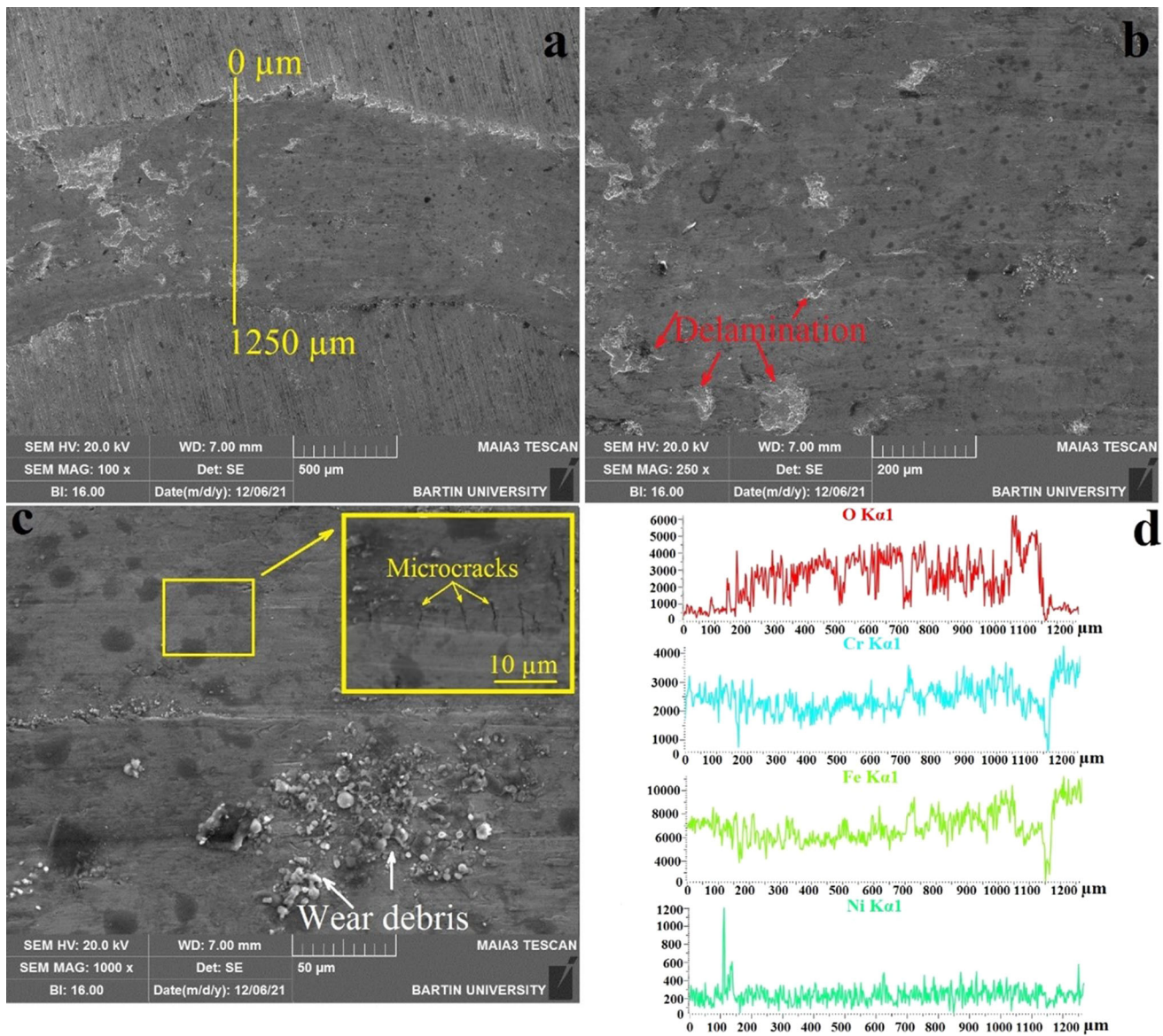
Fig. 17 Worn surface SEM micrograph of E10 (s = 170 mm/s, L = 17 N, T = 151 °C) experiment sample

Supplementary Figure IV, the appearance of less oxygen content in the parts of the broken glazed layer supports these claims. The difference of E19 from E17 is that the flat areas on the surface (oxidation) areas are larger. Indeed, the presence of oxidation was clearly observed along the wear trace as seen in the EDS mapping (Fig. SIV). The fact that oxidation occurred more in E19 than in E17 is a result of the wear process occurring at a higher temperature.

It is understood from the SEM wear photograph of the E4 (s = 170 mm/s, L = 8 N, T = 151 °C) sample given in Fig. 16 that the oxide layer is shed faster. As mentioned before, both the formation and shedding of the oxide layer formed on the surface is associated with the presence of many parameters. However, it can be said that the oxide layer is damaged more quickly at 150 °C. In addition, it is known that when this hard and brittle structure formed on the surface becomes a wear debris, it gets stuck between the interacting surfaces and causes an abrasion effect (Ref 46).

When the wear surface photographs of the E4 and E10 samples, which are tested at the same temperature value but different loads and different sliding speeds, are examined, although it can be said that the E4 sample (Fig. 16) is oxidation type wear mechanism is dominant. In particular, in the edge regions oxide layer is more stable but the oxide layers are broken in the central part of the wear trace. Since the force exerted by the interaction surface of the abrasive ball on the opposite surface in the central region of the trace will be greater, it can be predicted that the oxide layer will be broken in these regions.

Although E4 and E10 (s = 170 mm/s, L = 17 N, T = 151 °C) samples were tested at the same temperature, subjecting the E10 sample to a higher load completely changed the wear mechanism on the sample surface as seen in Fig. 17. It can even be said that the oxide layer, which is seen in E16 and completely covers the surface of the sample, is also present in this sample. In Fig. 17(d), the EDS line analysis taken from the wear trace region of the sample clearly shows the oxide density

on the surface. Likewise, partial spills are seen in the oxide layer covering the sample, but these spills are less than sample of the wear test done at 523 °C. According to these conclusions, load is just as significant as temperature in the formation of oxide and the progress of wear mechanisms. Moreover, the wear rate depends on the surface temperature condition (47).

4. Conclusions

As functions of load, sliding speed and temperature, response surfaces of CoF, efficient depth, track width, track cross section area and SWR were constructed with the reliabilities of 0.89, 0.98, 0.84, 0.95 and 0.95, respectively.

Reduced quadratic response surface model for CoF and reduced cubic model for efficient depth, track width, cross section area and SWR have developed. The effect of the independent factors on the responses is in a complex manner. These effects can be observed for any factor in the range of design area by means of 3D plots or 2D gradient maps which depicts response values with respect to values of independent parameters. Main conclusions from 3 D response surface plots can be driven as:

- In low temperatures with the increase in the load and speed influences negatively CoF but this changes with the increase in the temperature and CoF increases with increase in the load and the speed in temperatures near 600 °C.
- In low temperatures D values are low for low- and high-speed values but it gets bigger values about 200 mm/s. D changes in opposite manner in high temperatures. On the other hand, D increases with increase in load in low temperatures. In high temperatures it increases with increase in load in low speeds but this behavior changes with increase in the speed and gets opposite in 230 mm/s.
- In low temperatures w decreases for small loads and increases for bigger loads in low rates as the speed increases. These rates get bigger as the temperature increases. Change in w with the load is very limited in low temperatures. On the other hand w decreases with increase in the load very sharply in high temperatures and low speeds but the trend changes as the speed increases and w increases as load gets bigger and high temperatures and high speeds.
- Under low load values A almost stays constant as the speed changes in low temperatures but if the load value get higher A values are bigger in mid speeds from the ones low and high speeds. On the other hand, area does not change considerably with the load in low temperatures and low speeds but A decreases in a smooth way as the load increases in high speed and low temperature values but decrease in the A gets sharper in high temperatures.
- In low load values SWR increases as the speed increases and decreases with respect to mid speeds in high temperatures but SWR stay constant as the speed changes under low loads and low temperatures. On the other hand load and temperature has a little effect on SWR under higher loads. SWR increases with the increase in temperature in a low rate in low speeds but this increase gets very sharp in high speed especially under low loads.
- SEM analyses are conducted to validate response surface

results. It is seen from the SEM analyses that oxidation has a great influence on wear behavior of Incoloy 825.

References

1. M. J. Donachie, Superalloys- Source Book. *Metals Park OH Am. Soc. Metals*, 1984, p 424
2. M.J. Donachie and S.J. Donachie, *Superalloys: A Technical Guide*, ASM international, Netherlands, 2002
3. B. Geddes, H. Leon, and X. Huang, *Superalloys Alloying and Performance*, ASM International, Materials Park, Ohio, 2010
4. P. Song, M. Liu, X. Jiang, Y. Feng, J. Wu, G. Zhang, and L. Lou, Influence of Alloying Elements on Hot Corrosion Resistance of Nickel-Based Single Crystal Superalloys Coated with Na_2SO_4 Salt at 900° C, *Mater. Des.*, 2021, **197**, 109197
5. I. Gurrappa, Influence of Alloying Elements on Hot Corrosion of Superalloys and Coatings: Necessity of Smart Coatings for Gas Turbine Engines, *Mater. Sci. Technol.*, 2003, **19**(2), p 178–183
6. C.N. Chakravarthy, A Review on–Mechanical Properties and Composition of Incoloy alloy-825 reinforced Aluminum alloy-7075 metal powders, Methods & Applications, *PalArch's J. Archaeol. Egypt/ Egyptol.*, 2020, **17**(9), p 6947–6966
7. A.M. Ardali and B. Lotfi, Failure Analysis of Secondary Reformer Burner Nozzles Made from Incoloy 825 in an Ammonia Production Plant, *Eng. Fail. Anal.*, 2020, **118**, 104860
8. N. Sayyar, M. Shamanian, B. Niroumand, J. Kangazian, and J.A. Szpunar, EBSD Observations of Microstructural Features and Mechanical Assessment of INCOLOY 825 alloy/AISI 321 Stainless Steel Dissimilar Welds, *J. Manuf. Process.*, 2020, **60**, p 86–95
9. S. Venkataraman and D. Jakobi, A study on the microstructure, mechanical properties and corrosion resistance of centrifugally cast heavy wall thickness low carbon 46Ni-35Cr-9Mo alloy. In CORRO-SION 2017. OnePetro, 2017
10. X. Zhong, L. Huang, and F. Liu, Discontinuous Dynamic Recrystallization Mechanism and Twinning Evolution During Hot Deformation of Incoloy 825, *J. Mater. Eng. Perform.*, 2020, **29**(9), p 6155–6169
11. S. Liu, J. Huang, J. Zhang, X. Yu, and D. Fan, Microstructure, Mechanical Performance, and Corrosion Behavior of Electron Beam Welded Thick Incoloy 825 Joints, *J. Mater. Eng. Perform.*, 2021, **30**(5), p 3735–3748
12. P. George, K.L.D. Wins, D.E.J. Dhas, and P. George, Machinability, Weldability and Surface Treatment Studies of SDSS 2507 Material-A Review, *Mater. Today Proc.*, 2021, **46**, p 7682–7687
13. S. Sujai and K. Devendranath Ramkumar, Microstructure and Mechanical Characterization of Incoloy 925 Welds in the As-Welded and Direct Aged Conditions, *J. Mater. Eng. Perform.*, 2019, **28**(3), p 1563–1580
14. M. Sen and H.S. Shan, Analysis of Roundness Error and Surface Roughness in the Electro Jet Drilling Process, *Mater. Manuf. Processes*, 2006, **21**(1), p 1–9
15. F. Çavdar and E. Kanca, Utilization of Response Surfaces in the Optimization of Roll-Pass Design in Hot-Rolling, *Emerg. Mater. Res.*, 2020, **9**(4), p 1307–1318
16. J. Kangazian, N. Sayyar, and M. Shamanian, Influence of Microstructural Features on the Mechanical Behavior of Incoloy 825 Welds, *Metallogr. Microstruct. Anal.*, 2017, **6**(3), p 190–199
17. A. Günen and E. Kanca, Characterization of Borided Inconel 625 Alloy with Different Boron Chemicals, *Pamukkale Univ. J. Eng. Sci.*, 2017, **23**(4), p 411–416
18. J.Z. Yi, H.X. Hu, Z.B. Wang, and Y.G. Zheng, On the Critical Flow Velocity for Erosion-Corrosion of Ni-Based Alloys in a Saline-Sand Solution, *Wear*, 2020, **458–459**, p 203417. https://doi.org/10.1016/j.wear.2020.203417
19. F. Gong, J. Zhao, G. Liu, and X. Ni, Design and Fabrication of TiB2–TiC–Al2O3 Gradient Composite Ceramic Tool Materials Reinforced by VC/Cr_3C_2 Additives, *Ceram. Int.*, 2021, **47**, p 20341–20351
20. R.A. García-León, J. Martínez-Trinidad, I. Campos-Silva, U. Figueroa-López, and A. Guevara-Morales, Development of Tribological Maps on Borided AISI 316L Stainless Steel Under Ball-On-Flat Wet Sliding Conditions, *Tribol. Int.*, 2021, **163**, p 107161

21. R.A. García-León, J. Martínez-Trinidad, R. Zepeda-Bautista, I. Campos-Silva, A. Guevara-Morales, J. Martínez-Londoño, and J. Barbosa-Saldaña, Dry Sliding Wear Test on borided AISI 316L Stainless Steel Under Ball-On-Flat Configuration: A Statistical Analysis, *Tribol. Int.*, 2021, **157**, p 106885

22. Technical Bulletins for INCONEL® Alloys 2022. https://www.specialmetals.com/documents/technical-bulletins/incoloy/incoloy-alloy-825.pdf

23. Y.H. Lin, W.J. Deng, C.H. Huang, and Y.K. Yang, Optimization of Injection Molding Process for Tensile and Wear Properties of Polypropylene Components via Taguchi and Design of Experiments Method, *Polym.-Plast. Technol. Eng.*, 2007, **47**(1), p 96–105

24. M. Waseem, B. Salah, T. Habib, W. Saleem, M. Abas, and R. Khan et al., Multi-Response Optimization of Tensile Creep Behavior of PLA 3D Printed Parts Using Categorical Response Surface Methodology, *Polymers*, 2020, **12**(12), p 2962. https://doi.org/10.3390/polym12122962

25. T. Widyaningsih, S. Waziiroh, E. Wijayanti, and N. Maslukhah, Pilot Plant Scale Extraction of Black Cincau (Mesona palustris BL) Using Historical-Data Response Surface Methodology. Int Food Res J 2018, 25

26. H. Czichos Introduction to Friction and Wear. In *Composite Materials Series*, Vol. 1, pp. 1–23. Elsevier, 1986

27. D.Y. Pimenov, A.T. Abbas, and M.K. Gupta et al., Investigations of Surface Quality and Energy Consumption Associated with Costs and Material Removal Rate During Face Milling of AISI 1045 Steel, *Int J Adv Manuf Technol*, 2020, **107**, p 3511–3525

28. S. Mohammed, Z. Zhang, and R. Kovacevic, Optimization of Processing Parameters in Fiber Laser Cladding, *Int J Adv Manuf Technol*, 2020, **111**, p 2553–2568

29. S. Kumar, A. Bhattacharyya, D.K. Mondal, K. Biswas, and J. Maity, Dry Sliding Wear Behaviour of Medium Carbon Steel Against an Alumina Disk, *Wear*, 2011, **270**(5–6), p 413–421

30. X.H. Cui, S.Q. Wang, F. Wang, and K.M. Chen, Research on Oxidation Wear Mechanism of the Cast Steels, *Wear*, 2008, **265**(3–4), p 468–476

31. T.D. Vo, B. Tran, A.K. Tieu, D. Wexler, G. Deng, and C. Nguyen, Effects of Oxidation on Friction and Wear Properties of Eutectic High-Entropy Alloy AlCoCrFeNi2. 1, *Tribol. Int.*, 2021, **160**, p 107017

32. H. So, D.S. Yu, and C.Y. Chuang, Formation and Wear Mechanism of Tribo-Oxides and the Regime of Oxidational Wear of Steel, *Wear*, 2002, **253**(9–10), p 1004–1015

33. A. Tyagi, S. Banerjee, J. Cherusseri, and K. K. Kar, Characteristics of Transition metal Oxides, *Handbook of Nanocomposite Supercapacitor Materials I: Characteristics*. Springer International Publishing, Cham, 2020, p 91–123

34. C. Trevisiol, A. Jourani, and S. Bouvier, Effect of Hardness, Microstructure, Normal Load and Abrasive Size on Friction and on Wear Behaviour of 35NCD16 Steel, *Wear*, 2017, **388**, p 101–111

35. A. T. Fromhold, Theory of Metal Oxidation. Vol. 1: Fundamentals. Amsterdam: Elsevier; 1976

36. M.A. Maleque, H.H. Masjuki, and A.S.M.A. Haseeb, Effect of Mechanical Factors on Tribological Properties of Palm Oil Methyl Ester Blended Lubricant, *Wear*, 2000, **239**(1), p 117–125

37. J. Glascott, G.C. Wood, and F.H. Stott, The Influence of Experimental Variables on the Development and Maintenance of Wear-Protective Oxides During Sliding of High-Temperature Iron-Base Alloys, *Proc. Inst. Mech. Eng. C J. Mech. Eng. Sci.*, 1985, **199**(1), p 35–41

38. J.H. Kang, I.W. Park, J.S. Jae, and S.S. Kang, A Study on a Die Wear Model Considering Thermal Softening:(I) Construction of the Wear Model, *J. Mater. Process. Technol.*, 1999, **96**(1–3), p 53–58

39. M. Awang, A.A. Khalili, and S.R. Pedapati, A Review: Thin Protective Coating for Wear Protection in High-Temperature Application, *Metals*, 2019, **10**(1), p 42

40. S.A.A. Dilawary, A. Motallebzadeh, E. Atar, and H. Cimenoglu, Influence of Mo on the High Temperature Wear Performance of NiCrBSi Hardfacings, *Tribol. Int.*, 2018, **127**, p 288–295

41. A. Motallebzadeh, E. Atar, and H. Cimenoglu, Sliding Wear Characteristics of Molybdenum Containing Stellite 12 Coating at Elevated Temperatures, *Tribol. Int.*, 2015, **91**, p 40–47

42. S.Q. Wang, M.X. Wei, F. Wang, and Y.T. Zhao, Transition of Elevated-Temperature Wear Mechanisms and the Oxidative Delamination Wear in Hot-Working Die Steels, *Tribol. Int.*, 2010, **43**(3), p 577–584

43. R. Mnif, Z. Baccouch, R. Elleuch, and C. Richard, Investigations of High Temperature Wear Mechanisms for Tool Steel Under Open-Sliding Contact, *J. Mater. Eng. Perform.*, 2014, **23**(8), p 2864–2870

44. A. Günen and A. Çürük, Properties and High-Temperature Wear Behavior of Remelted NiCrBSi Coatings, *JOM*, 2020, **72**(2), p 673–683

45. R.A. García-Léon, J. Martínez-Trinidad, A. Guevara-Morales, I. Campos-Silva, and U. Figueroa-López, Wear Maps and Statistical Approach of AISI 316L Alloy Under Dry Sliding Conditions, *J. Mater. Eng. Perform.*, 2021, **30**(8), p 6175–6190

46. D.V. De Pellegrin, A.A. Torrance, and E. Haran, Wear Mechanisms and Scale Effects in Two-Body Abrasion, *Wear*, 2009, **266**(1–2), p 13–20

47. Y. Wang, Z. Jia, Z. Ji, B. Wei, Y. Heng, and D. Liu, Determining the Wear Behavior of H13 Steel Die During the Extrusion Process of Pure Nickel, *Eng. Fail. Anal.*, 2022, **134**, p 106053